Sedimentology (2007) **54,** 1007–1031 doi: 10.1111/j.1365-3091.2007.00870.x

Dolomite formation in the dynamic deep biosphere: results from the Peru Margin

PATRICK MEISTER*†, JUDITH A. MCKENZIE†, CRISOGONO VASCONCELOS†, STEFANO BERNASCONI†, MARTIN FRANK‡, MARCUS GUTJAHR§ and DANIEL P. SCHRAG¶

**Department of Earth Sciences, USC, 3651 Trousdale Parkway, Los Angeles, CA 90089-0740, USA (E-mail: patrick.meister@alumni.ethz.ch)*

†ETH-Zürich, Geological Institute, 8092 Zürich, Switzerland

‡IFM-GEOMAR, Leibnitz Institute for Marine Sciences, University of Kiel, Wischhofstrasse 1-3, 24148 Kiel, Germany

§ETH-Zürich, Institute for Isotope Geology and Mineral Resources, 8092 Zürich, Switzerland

¶Department of Earth and Planetary Sciences, Harvard University, 20 Oxford St, Cambridge, MA 02138, USA

ABSTRACT

Early diagenetic dolomite beds were sampled during the Ocean Drilling Programme (ODP) Leg 201 at four reoccupied ODP Leg 112 sites on the Peru continental margin (Sites 1227/684, 1228/680, 1229/681 and 1230/685) and analysed for petrography, mineralogy, $\delta^{13}C$, $\delta^{18}O$ and $^{87}Sr/^{86}Sr$ values. The results are compared with the chemistry, and $\delta^{13}C$ and $^{87}Sr/^{86}Sr$ values of the associated porewater. Petrographic relationships indicate that dolomite forms as a primary precipitate in porous diatom ooze and siliciclastic sediment and is not replacing the small amounts of precursor carbonate. Dolomite precipitation often pre-dates the formation of framboidal pyrite. Most dolomite layers show $^{87}Sr/^{86}Sr$-ratios similar to the composition of Quaternary seawater and do not indicate a contribution from the hypersaline brine, which is present at a greater burial depth. Also, the $\delta^{13}C$ values of the dolomite are not in equilibrium with the $\delta^{13}C$ values of the dissolved inorganic carbon in the associated modern porewater. Both petrography and $^{87}Sr/^{86}Sr$ ratios suggest a shallow depth of dolomite formation in the uppermost sediment (<30 m below the seafloor). A significant depletion in the dissolved Mg and Ca in the porewater constrains the present site of dolomite precipitation, which co-occurs with a sharp increase in alkalinity and microbial cell concentration at the sulphate–methane interface. It has been hypothesized that microbial 'hot-spots', such as the sulphate–methane interface, may act as focused sites of dolomite precipitation. Varying $\delta^{13}C$ values from −15‰ to +15‰ for the dolomite are consistent with precipitation at a dynamic sulphate–methane interface, where $\delta^{13}C$ of the dissolved inorganic carbon would likewise be variable. A dynamic deep biosphere with upward and downward migration of the sulphate–methane interface can be simulated using a simple numerical diffusion model for sulphate concentration in a sedimentary sequence with variable input of organic matter. Thus, the study of dolomite layers in ancient organic carbon-rich sedimentary sequences can provide a useful window into the palaeo-dynamics of the deep biosphere.

Keywords Carbon isotopes, deep biosphere, dolomite, Peru Margin, strontium isotopes, sulphate–methane interface.

INTRODUCTION

The occurrence of dolomite associated with organic carbon-rich continental margin sediments was recognized during the Deep-Sea Drilling Program (DSDP) Legs 63 and 64 on the California Margin and in the Gulf of California, respectively (Pisciotto & Mahoney, 1981; Kelts & McKenzie, 1982). A similar association has also been described from the geological record in California in the Miocene Monterey Formation (Murata *et al.*, 1969; Garrison & Graham, 1984; Burns *et al.*, 1988; Compton, 1988). Although many hypotheses have been developed, the controlling factors for the formation of deep-sea diagenetic dolomite are still not fully understood. Based on the concept of Claypool & Kaplan (1974), the carbon isotopic composition of the dolomite indicates the diagenetic conditions under which precipitation occurs. Negative $\delta^{13}C$ values indicate precipitation in association with bacterial sulphate reduction, whereas positive values indicate methanogenic microbial activity. Kelts & McKenzie (1984) concluded that the type of dolomite (methanogenic vs. sulphate reducing) is controlled by sedimentation rate, limiting the diffusive transport and penetration depth of SO_4^{2-} ions, while organic matter degradation increases the alkalinity of the porewater, inducing carbonate precipitation (Burns *et al.*, 1988; Compton, 1988). Baker & Kastner (1981) proposed a sulphate inhibition model, in which removal of sulphate ions by bacterial sulphate reduction facilitates dolomite precipitation. This model is based on high-temperature experiments, but its validity at low temperatures is still not confirmed. Vasconcelos *et al.* (1995) and Warthmann *et al.* (2000) demonstrated that dolomite precipitates in anaerobic culture experiments at low temperatures, providing strong evidence that sulphate-reducing bacteria play a key role in overcoming the kinetic barrier of dolomite formation. Nevertheless, the mechanism for dolomite formation in deep-sea sediments remains controversial, and the precise factors controlling this process in natural environments remain unknown.

One classic site for the study of hemipelagic and 'deep-sea' (the term 'deep-sea' dolomite is used to distinguish it from dolomite formed in restricted evaporative environments, such as 'sabkha dolomite') dolomite formation is the Peru continental margin, where dolomite was first recovered by deep-sea dredging during the Nazca Plate Project (Kulm *et al.*, 1981, 1984) and during the Ocean Drilling Programme (ODP) Leg 112 (Suess *et al.*, 1988). Different dolomite assemblages with variable $\delta^{13}C$ values ranging from −14 to +17‰ were described at different sites, which were related to the different tectono-sedimentary settings (Kulm *et al.*, 1984). Besides micritic early diagenetic dolomite, Thornburg & Suess (1990) also distinguished four different exotic cements. Low-Mg calcite, with a $\delta^{18}O$ value of −7·5‰, was interpreted as being formed by meteoric diagenesis during Eocene uplift. Low-Mg calcite cements in the late Miocene accretionary prism, showing lowered Mg/Ca ratios and $\delta^{18}O$ values, were considered to be cements precipitated from fluid influenced by basaltic alteration at depth. Micritic high-Mg calcite, with extremely low $\delta^{13}C$ (−37·3‰), provided evidence for venting of methane-charged waters at the seafloor. Enriched $\delta^{18}O$ values (+6·6‰) in dolomites from the continental shelf are consistent with the presence of hypersaline fluids that were concentrated in restricted lagoons behind an outer shelf basement ridge during the late Miocene. These previous studies, however, did not integrate fully the geochemical data from the dolomites with the modern porewater geochemistry and with the modern geobiochemical processes occurring in the deep sub-seafloor biosphere.

In this study, dolomite samples recovered during ODP Leg 201 from four re-occupied sites of ODP Leg 112 in open marine, continental shelf to deep-sea sedimentary sequences on the Peru Margin are investigated. ODP Leg 201 was dedicated to the study of microbial life deeply buried below the seafloor (the so-called 'deep biosphere'). During Leg 201, a highly active 'deep biosphere' was detected at different locations on the Peru Margin (D'Hondt *et al.*, 2003, 2004; Mauclaire *et al.*, 2004; Parkes *et al.*, 2005; Schippers *et al.*, 2005; Biddle *et al.*, 2006; Inagaki *et al.*, 2006; Schippers & Neretin, 2006) providing a new context in which dolomite formation in a deep-sea hemipelagic environment can be evaluated. The studied dolomite samples were systematically analysed for petrographic relationships, mineralogy, $\delta^{13}C$, $\delta^{18}O$, and $^{87}Sr/^{86}Sr$ values. Comparison of $^{87}Sr/^{86}Sr$ and $\delta^{13}C$ values of dolomite and modern porewater, petrographic relationships, and Mg/Ca concentrations in the porewater, constrains the depth of dolomite formation in the subsurface, which is crucial for the understanding of the *in situ* geochemical environment associated with dolomite formation. Sulphate and microbial cell concentrations were also available from the shipboard analyses. A

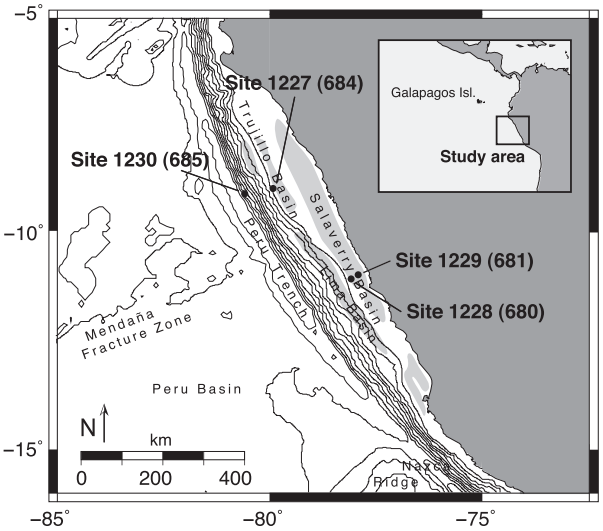

Fig. 1. Map of the Peru Margin showing locations of the five studied ODP Leg 201 drill sites (Sites 1227, 1228, 1229 and 1230), which correspond to reoccupied ODP Leg 112 sites (Sites 684, 680, 681 and 685). Shaded areas mark the ancient upper slope and shelf basins, which were infilled with late Tertiary and Quaternary sediments. Bathymetry is shown by isobaths with an equidistance of 500 m.

numeric diffusion model for SO_4^{2-} is used to explain the dynamics of porewater SO_4^{2-} profiles through time. Carbon isotope values from the dolomite ($\delta^{13}C_{DOL}$) provide an important record of microbial activity in the past, during times when the dolomite precipitated. With this approach, dolomite formation is examined in a dynamic environment, where physico-chemical processes and microbial activity are interacting.

STUDY AREA

The locations of the four sites drilled during ODP Leg 201 on the Peru Margin are shown in Fig. 1 (D'Hondt *et al.*, 2003). ODP Sites 1228 and 1229, reoccupied ODP Sites 680 and 681, are located on the Peru shelf in water depths of 250 and 150 m below sea-level (mbsl) respectively. ODP Site 1227 (ODP Site 684) was drilled at 430 mbsl on the upper slope, and ODP Site 1230 (ODP Site 685) on the lower slope at 5086 mbsl near the Peru Trench. The Peru continental margin is characterized by active subduction tectonics with the shelf subdivided into different sets of fore-arc basins, which are separated by topographic highs. On these ridges, sediment bypass or erosion occurred, and dolomite, as old as Miocene in age, is exposed on the seafloor (Kulm *et al.*, 1984). The drilled sites were generally located in a central position within the different basins, such as the Salaverry and Lima basins (Fig. 1), which were infilled by more continuous sedimentation. During a major Eocene orogenic phase, large areas of the Peruvian shelf were uplifted and exposed above sea-level. This tectonic event is documented by an unconformity, which was observed at the different Leg 112 sites (Suess *et al.*, 1988). Also, a major hiatus is present in the middle Miocene of the upper slope and shelf sites indicating a second phase of uplift (Suess *et al.*, 1988). During times of tectonic uplift, shelf basins were separated from the open ocean by the structural highs and restricted hypersaline conditions prevailed, leading to the formation of hypersaline brine (Thornburg & Suess, 1990). Such brine was recovered from deep drill cores at the shelf sites (Suess *et al.*, 1988). Late Miocene subsidence is more pronounced south of the Mendaña Fracture Zone, in the Lima Basin, whereas the Trujillo Basin in the north (Site 1227/684) shows condensed Pliocene–Pleistocene stratigraphy (Suess *et al.*, 1988).

The sediments of the Peru Margin consist mainly of organic carbon-rich diatom ooze with variable amounts of detrital clay, silt and sand. Total inorganic carbon content is generally around 1 wt%; however, in several horizons of Sites 1227 and 1228 values scatter up 2 or 3 wt% (Meister *et al.*, 2005). The sedimentary carbonate most commonly consists of foraminiferal tests. Sedimentation rates are variable between the different sites with a Quaternary section of about 12 m at Site 1227, 56 m at Site 1228, 180 m at Site 1229 and 216 m at Site 1230 (D'Hondt *et al.*, 2003). These sediments are the product of strong upwelling along the Peruvian coast with some input of terrigenous material. High productivity leads to an oxygen minimum zone, located in the water column between 150 and 400 mbsl (Suess *et al.*, 1988), which impinges on the seafloor at the shelf and upper slope sites. Palaeobathymetry reconstructed by Resig (1990) indicates lower neritic to upper bathyal conditions throughout the Pliocene to Holocene for the shelf and upper slope sites. However, sea-level variations strongly influenced sedimentation at the shelf sites. During lowstands, siliciclastic input increased and upwelling cells migrated seaward with the oxygen minimum zone impinging on the seafloor further away from the modern coast (Suess, von Huene, *et al.*, 1988). Ten metres scale cyclicity in sediment composition and total organic carbon (TOC) content has been related to such glacial-interglacial sea-level variations (Emeis & Morse, 1990; Wefer *et al.*, 1990).

Porewater chemistry from Leg 201 indicates high sulphate reducing and methanogenic activity at the Peru Margin drill sites. At the trench site (Site 1230/685), sulphate is consumed within the uppermost 10 m below seafloor (mbsf) with high production of methane and the presence of gas hydrates. However, at the shelf sites, the sulphate–methane interface (SMI) occurs much deeper, around 30 mbsf (Sites 1227/684 and 1229/681), which would not be predicted considering the high TOC content of these upwelling-sediments. At Site 1228/680, no SMI is present at all, but the SO_4^{2-} concentration reaches a minimum of about 3 mM near 40 mbsf. Methane occurs only in μM concentrations, which is not sufficient to maintain an upward flux high enough to remove all the sulphate by anaerobic methane oxidation (AMO). Sulphate also diffuses upward from the brine producing an increase in SO_4^{2-} concentration below 40 mbsf at Site 1228 and a second lower SMI at 90 mbsf at Site 1229 (D'Hondt *et al.*, 2003).

METHODS

Forty dolomite samples from Sites 1227, 1228, 1229 and 1230 were systematically sampled onboard the *JOIDES Resolution* during ODP Leg 201. Ten ODP Leg 112 samples from the core repository were also investigated. For each dolomite sample an additional sample was collected from the surrounding soft sediment (mostly diatomaceous mud with some friable dolomite) for comparison. Thin sections, made from lithified samples, were stained for calcite using the method of Dickson (1966) and analysed using a petrographic microscope. For description of crystallization textures and fabrics of dolomite, the terminology of Friedman (1965) was used. Additionally, cold cathode luminescence was applied to detect different generations of carbonate cements. Bulk samples of dolomite nodules and surrounding sediment were powdered and mineralogically analysed using a Scintag XDS 2000 X-ray diffractometer (Scintag Inc., CA, USA). The samples were scanned continuously at $1° \text{ min}^{-1}$ from 10° to 70° with Cu-Kα radiation. Dolomite stoichiometry was calculated from the displacement of the (104) peak using the equation of Lumsden (1979).

The carbon and oxygen isotope compositions of powdered bulk dolomite samples, as well as small microdrilled subsamples from thin section cuttings, were analysed in the Stable Isotope Laboratory at the Geological Institute of the ETH Zürich. Samples were dissolved using an on-line common acid method and a VG PRISM mass spectrometer (Scientific Instrument Services, NJ, USA). The reaction time was set at 10 min. The analytical precision of the mass spectrometer is ±0·1‰ for $\delta^{13}C$ and ±0·2‰ for $\delta^{18}O$. All $\delta^{18}O$ values have been corrected for dolomite–phosphoric acid fractionation at 90 °C using the fractionation factor of 1·0093 (Rosenbaum & Sheppard, 1986). The $\delta^{13}C$ and $\delta^{18}O$ values of the carbonates are given relative to the Vienna Pedee Belemnite Standard (VPDB). Reproducibility of repeated measurements is ±0·41‰ for $\delta^{13}C$ and ±0·39‰ for $\delta^{18}O$. The relatively low reproducibility (compared with precision) is due to inhomogeneity of the samples, which is expressed in the wide range of values measured in microdrilled subsamples across different layers. However, no systematic variation was observed by comparing different profiles across the dolomite layers. Calcite concentration was 5% or less in all samples, and, therefore, the influence of 'marine' calcite is small compared with the high variations of the $\delta^{13}C$ values. The $\delta^{13}C$ and $\delta^{18}O$ data are listed in Table 1. For $\delta^{13}C$ measurements of dissolved inorganic carbon (DIC) (Table 3), samples were acidified with orthophosphoric acid, and the evolved CO_2 measured on an Optima gas-source mass spectrometer (Scientific Instrument Services, NJ, USA). Precision of the $\delta^{13}C$ measurements of DIC is ±0·1‰. Eight samples were selected for Sr isotope analysis (Table 1). A total of 1·5 g of each powdered dolomite sample was purified in 10 ml of 0·1 M ethylenediaminetetraacetic acid (EDTA) solution (pH 6·3) and shaken overnight to remove small amounts of biogenic calcite. XRD analysis before and after EDTA treatment confirmed the efficient removal of calcite. Thirty to 50 mg of purified dolomite was leached in 0·5 ml 1 M acetic acid or Na-acetate buffer. Residual material was removed by centrifugation and again checked by XRD. Both leaching agents successfully removed the major part of dolomite in the sample. Control samples containing no dolomite showed values that are strongly offset from the dolomite samples, as well as the modern porewater concentrations. These samples showed less radiogenic signals (0·707217) when acetic acid was used and more radiogenic signals (0·711734) when Na-acetate buffer was used as a leaching agent (Table 1). This difference is probably due to leaching of Sr from different mineral fractions. However, dolomitic samples contain one to two orders of

Table 1. Carbon, oxygen and strontium isotope values of dolomite, calcite and unlithified (soft) sediment from ODP Leg 201, Peru Margin.

Core-section interval (cm)	Depth (mbsf)	$\delta^{13}C$ (‰PDB)	$\delta^{18}O$ (‰PDB)	Normalized $^{87}Sr/^{86}Sr$, Kr, Rb corrected	2σ, internal error (ppm)
Soft sediment					
681A-1H-1, 0–150	1·5	1·39	2·63		
681A-3H-1, 100–130	17·0	−3·87	−1·46		
681A-3H-6, 55–93	24·1	−7·51	4·50		
681A-11H-2, 130–150	94·8	−7·35	1·00		
681A-14X-2, 60–95	122·6	−4·71	−0·37		
681A-18X-CC, 0–18	158·7	−7·78	1·97		
685A-2H-2, 45–60	6·5	−10·95	1·77		
685A-2H-2, 60–95	6·2	−4·51	1·12		
1227A-11H-1, 40–50	91·5	0·63	1·81		*
1227A-12H-1, 79–91	101·4	7·75	2·62		
1227D-5H-1, 18–24	36·2	−11·76	1·28		
		4·62	4·64		†
1228A-6H-6, 62–70	51·2	−10·88	3·67		
1228A-8H-4, 144–150	67·8	−7·70	2·27		
1228A-22H-1, 22–26	185·6	−3·63	2·96		
1228B-6H-2, 92–109	47·2	−11·66	4·09		
1228B-6H-4, 68–83	50·0	−9·03	2·96		
1229A-1H-3, 85–91	3·9	−7·22	2·13		
1229A-3H-1, 53–59	14·9	−6·50	4·54		
1229A-4H-2, 93–97	26·3	−1·27	4·47		
1229A-5H-3, 80–86	37·2	4·83	4·21		
1229A-8H-1, 57–72	59·5	−12·89	2·80		
1229A-8H-4, 84–99	64·2	−17·01	4·21		
1229A-10H-1, 93–114	80·3	−9·55	3·96		
1229A-12H-4, 36–50	100·8	−6·70	−0·14		
1229A-13H-2, 106–118	110·5	−4·50	2·77		
1229D-8H-2, 105–120	61·4	−12·48	3·92		
1229A-8H-4, 82–84	64·2	−12·48	2·90	0·711734	±107‡§
				0·707217	±14§
				0·707845	±37§
Dolomite					
681A-3H-6, 55–93	24·1	−9·34	4·26		
681A-11H-2, 130–150	94·8	−10·16	3·55		
681A-18X-CC, 0–18	158·7	−9·15	3·27		
685A-2H-2, 45–60	6·5	−30·01	4·53		
		−32·79	4·06		
		−36·15	4·17		
		−25·47	4·40		
		−35·85	4·42		
1227A-8H-CC, 30–36	62·9	−5·43	3·47	0·708663	±50‡
		−1·68	3·52		
		−11·43	4·34		
		−13·19	3·47		
		−2·13	3·29		
		−8·76	3·44		
1227A-11H-1, 40–50	91·5	11·50	3·44		
1227A-12H-1, 79–91	101·4	9·63	3·54	0·709108	±42‡
		9·84	3·06		
		9·82	3·49		
1227A-13H-1, 28–30	110·4	10·63	3·68		
		10·34	3·41		
		11·09	3·32		
1228A-5H-1, 5–10	33·5	−11·19	4·48	0·709284	±46‡
		−11·36	4·26		

Table 1. Continued

Core-section interval (cm)	Depth (mbsf)	$\delta^{13}C$ (‰PDB)	$\delta^{18}O$ (‰PDB)	Normalized $^{87}Sr/^{86}Sr$, Kr, Rb corrected	2σ, internal error (ppm)
		−11·31	4·30		
		−11·21	4·37		
		−11·28	4·43		
		−11·18	4·21		
1228A-6H-6, 62–70	51·2	−10·63	3·83		
		−10·59	3·52		
		−10·50	3·86		
		−10·59	3·90		
		−9·87	3·59		
1228A-8H-4, 144–150	67·8	−3·39	3·12	0·709120	±52‡
1228A-22H-1, 22–26	185·6	1·51	3·23	0·709020	±54‡
		0·31	3·34		
		0·91	3·42		
		1·03	3·46		
		1·62	3·31		
1228B-6H-2, 97–101	47·3	−11·75	3·91		
		−11·73	4·04		
		−11·84	3·95		
		−11·69	3·92		
1228B-6H-4, 73–77	50·0	−10·63	4·01		
1229A-4H-1, 18–19	24·1	−9·93	4·15	0·709093	±14
				0·709114	±14
		−9·81	4·02		
		−9·70	4·16		
1229A-4H-2, 95–96	26·4	−0·44	4·55		
		−4·71	4·02		
		−0·53	4·43		
		−3·09	4·38		
1229A-5H-4, 81–84	38·7	2·68	4·15	0·709044	±12
				0·709025	±12
		2·91	0·08		
		5·04	3·95		
		3·84	4·18		
1229A-8H-1, 55–64	59·5	−13·61	4·15		
1229A-8H-1, 55–64		−7·65	2·72		
		−9·40	1·73		
1229A-10H-1, 133–136	80·7	−9·68	3·50	0·709027	±13
				0·709002	±11
		−9·26	3·95		
		−10·18	4·25		
1229A-11H-1, 31–34	89·2	−6·22	4·56		
		−0·53	4·48		
		−3·54	4·49		
		−4·22	4·50		
1229A-12H-1, 64–65	99·0	−8·90	3·16		
1229A-12H-2, 86–88	100·8	−6·99	4·28		
		−6·49	4·21		
		−5·06	3·77		
		−7·59	3·39		
1229A-12H-5, 68–69	105·1	5·72	3·89		
		4·00	3·80		
		6·09	4·03		
		6·09	3·96		
1229A-13H-2, 109–112	110·5	−0·70	2·78	0·709033	±56‡
				0·708825	±12
				0·708821	±11

Table 1. Continued

Core-section interval (cm)	Depth (mbsf)	$\delta^{13}C$ (‰PDB)	$\delta^{18}O$ (‰PDB)	Normalized $^{87}Sr/^{86}Sr$, Kr, Rb corrected	2σ, internal error (ppm)
		−2·34	3·15		
		−6·62	2·76		
		−4·64	3·17		
1229A-14H-3, 135	121·8	−9·05	2·35		
1229D-2H-1, 71–72	7·5	−7·34	4·28		
1229D-5H-3, 24–29	38·5	3·53	4·29		
		−0·36	4·13		
		4·02	4·39		
1229D-8H-2, 105–120	61·4	−12·80	4·32		
		−11·93	4·00		
		−13·39	4·37		
		−8·54	2·88		
Calcite					
1227A-4H-5, 62	30·9	−17·76	2·69		
1227A-11H-1, 21–24	91·3	−0·71	1·56		
1227A-11H-1, 40–50	91·5	−15·02	2·55		

*Apatite.
†Baryte.
‡Leached with Na-acetate buffer for Sr analysis.
§Non-carbonaceous sample.

magnitude higher Sr concentrations, and, thus, the leaching method has no significant effect on the values of dolomite samples. Chemical separation and purification followed standard procedures for Sr (Horwitz *et al.*, 1991) for both dolomite and porewater samples. Strontium isotopic compositions were measured on a Nu Instruments (Nu Instruments Ltd., Wrexham, UK) multiple collector inductively coupled plasma mass spectrometer (MC-ICPMS). Sr isotope ratio measurements were corrected for Kr interference and measured $^{87}Sr/^{86}Sr$ were normalized to $^{88}Sr/^{86}Sr = 8{\cdot}3752$ to correct for instrumental mass bias. As Rb was efficiently separated by column chemistry, less than 1% of the measured radiogenic ^{87}Sr was Rb, which was neglected. The 2σ external precision for the different sessions of $^{87}Sr/^{86}Sr$ measurements varied between 30 and 78 ppm for repeated measurements of the same NIST NBS987 standard. All ratios were normalized to a given value of 0·710245 for NB8987. In-run precision for each sample was better than the external reproducibility. The strontium isotope data for dolomite and porewater are included in Tables 1 and 2 respectively. Results of the porewater analysis correlate well with the porewater Sr-data of Kastner *et al.* (1990) and the two data sets were combined (Fig. 8). The reconstructed

Table 2. $^{87}Sr/^{86}Sr$ data for porewaters from ODP Sites 1229 and 1230.

Core-section interval (cm)	Depth (mbsf)	$^{87}Sr/^{86}Sr$	2 s internal error (ppm)
201-1229A-1H-1, 135–150	1·4	0·709157	±12*
1229A-3H-5, 135–150	21·8	0·708959	±15*
1229A-4H-5, 135–150	31·3	0·708922	±14*
1229A-6H-3, 0–15	42·9	0·708840	±11*
1229A-13H-1, 135–150	109·3	0·708457	±14*
1229A-18H-1, 135–150	156·8	0·708121	±14*
1229A-22H-1, 135–150	186·3	0·707998	±13*
201-1230A-12-2, 135–150	92·2	0·709064	±13
1230A-22-1, 85–90	169·2	0·709215	±12
1230A-24-2, no interval	188·8	0·709296	±16
1230B-1-1, 80–95	0·8	0·709191	±14
1230B-5-3, 135–150	28·4	0·709135	±17

*Frozen sample.

Table 3. Carbon isotope values of dissolved inorganic carbon (DIC) and Mg^{2+} and Ca^{2+} concentrations of ODP Leg 201 porewater.

Site	Hole	Core	Sect	Int. top (cm)	Int. bottom (cm)	Depth (mbsf)	$\delta^{13}C$ (‰PDB)	Mg^{2+} (mM)	Ca^{2+} (mM)
1227	A	1	1	135	150	1·35	−10·2	45·03	8·60
1227	A	1	2	135	150	2·85	−12·4	44·04	6·99
1227	A	1	3	135	150	4·35	−12·9		
1227	A	2	1	135	150	6·95	−13·0		
1227	A	2	2	135	150	8·45	−14·7		
1227	A	2	3	135	150	9·95	−12·2		
1227	A	2	5	135	150	12·95	−19·3	43·28	3·23
1227	A	2	6	135	150	14·45	−19·6		
1227	A	3	1	135	150	16·45	−19·4		
1227	A	3	2	135	150	17·95	−20·9	43·76	3·62
1227	A	3	3	135	150	19·45	−18·2		
1227	A	3	4	135	150	20·95	−20·4		
1227	A	3	5	135	150	22·45	−21·1	47·75	7·43
1227	A	3	6	135	150	23·95	−19·5	48·74	7·78
1227	A	4	1	102	117	25·62	−21·7	48·05	5·33
1227	A	4	5	95	110	31·21	−18·4	45·60	8·06
1227	A	5	1	135	150	35·45	−24·0	50·29	8·55
1227	A	5	2	135	150	36·95	−24·1	51·67	8·47
1227	A	5	3	135	150	38·45	−24·6	51·16	7·48
1227	A	5	4	135	150	39·95	−25·4		
1227	A	5	5	135	150	41·45		53·01	10·59
1227	A	5	6	135	150	42·95	−23·7	50·61	7·53
1227	A	6	1	135	150	44·95	−22·7	50·08	11·08
1227	A	6	4	135	150	49·45	−23·5	53·78	12·08
1227	A	7	1	135	150	54·45	−10·5	58·51	12·43
1227	A	7	2	135	150	55·95	−13·3	57·79	12·99
1227	A	9	1	135	150	73·45	−10·4	60·00	27·14
1227	A	9	3	135	150	76·45	1·5	59·80	17·05
1227	A	10	2	135	150	84·45	−5·7	59·05	18·13
1227	A	10	4	135	150	87·45		61·43	20·28
1227	A	11	2	135	150	93·95	−6·2	60·15	25·54
1227	A	12	2	135	150	103·50	−5·1	38·65	30·67
1227	A	12	4	135	150	106·50	−4·5	61·15	30·36
1227	A	13	1	135	150	111·50	−4·6	63·25	20·85
1227	A	13	4	135	150	116·00	−3·6	65·93	25·41
1227	A	14	1	135	150	121·00	−3·4	46·18	18·90
1227	A	17	1	85	100	133·00	−2·1	52·61	19·35
1227	A	18	2	135	150	144·30	−3·7	52·14	22·01
1227	A	18	3	0	20	144·50	−2·2	72·50	30·22
1227	D	1	1	0	1	0·00	−4·6	45·48	8·90
1227	D	1	1	0	15	0·00	−5·5	48·68	9·41
1227	D	1	1	60	75	0·60	−8·4	48·80	9·49
1227	D	1	1	100	115	1·00	−9·0	48·69	9·33
1227	D	1	2	30	45	2·09	−11·6	44·46	8·42
1227	D	4	1	135	45	27·85	−24·7	44·49	5·34
1227	D	4	2	135	150	29·35	−13·9	48·51	3·74
1227	D	4	3	135	150	30·85	−20·7	49·19	8·58
1227	D	4	4	135	150	32·35	−17·4	55·31	8·68
1227	D	4	5	135	150	33·85	−17·0	47·23	2·98
1227	D	4	6	135	150	35·35	−5·5	52·90	9·16
1227	D	5	1	135	150	37·35	−23·6	51·54	10·22
1227	D	5	2	135	150	38·85	−21·3	52·70	6·01
1227	D	5	3	135	150	40·35	−16·0	50·60	10·63
1227	D	5	4	135	150	41·85	−21·7	52·32	10·00
1227	D	5	5	91	106	42·91	2·7		
1227	D	6	2	0	20	47·00	−0·1		

Table 3. Continued

Site	Hole	Core	Sect	Int. top (cm)	Int. bottom (cm)	Depth (mbsf)	$\delta^{13}C$ (‰PDB)	Mg^{2+} (mM)	Ca^{2+} (mM)
1227	D	8	2	109	124	65·93	−1·9	52·00	12·15
1228	A	1	1	126	141	1·26	−14·2	52·00	8·37
1228	A	1	2	135	150	2·76	−11·5		
1228	A	1	3	135	150	4·26	−11·2	48·30	7·30
1228	A	2	1	135	150	6·25	−13·4	42·38	6·80
1228	A	2	3	0	15	7·90	−12·9	45·97	7·65
1228	A	2	3	135	150	9·25	−11·9	46·26	7·87
1228	A	2	5	135	150	12·25	−11·4	43·37	4·55
1228	A	3	1	135	150	15·75	−8·8	38·73	6·54
1228	A	3	3	135	150	18·75	−11·1	45·12	7·74
1228	A	3	5	135	150	21·75	−13·3	45·22	7·85
1228	A	4	1	135	150	25·25	−10·8		
1228	A	4	3	135	150	28·25	−11·8	44·52	6·90
1228	A	4	5	135	150	31·25		44·60	8·25
1228	A	5	1	135	150	34·75	−11·2	43·94	5·78
1228	A	5	3	135	150	37·75	−11·9	46·01	7·57
1228	A	5	4	135	150	39·25		45·01	8·13
1228	A	6	1	135	150	44·25	−10·1	46·91	8·44
1228	A	6	3	135	150	47·25	−12·2	46·91	9·15
1228	A	7	1	135	150	53·75	−11·5	49·32	10·08
1228	A	7	3	135	150	56·75	−11·3	50·21	10·71
1228	A	7	5	135	150	59·75	−10·4	50·58	11·00
1228	A	8	1	135	150	63·25	−9·5	54·04	10·44
1228	A	8	3	135	150	66·25	−12·6	54·80	12·18
1228	A	8	5	135	150	69·25	−9·6	56·00	10·93
1228	A	8	5	135	150	69·25	−9·6		
1228	A	9	1	135	150	72·75	−10·8	57·92	13·17
1228	A	9	1	135	150	72·75	−10·8		
1228	A	9	1	135	150	72·75	−10·8		
1228	A	9	3	135	150	75·75	−13·5	58·29	13·24
1228	A	10	1	135	150	82·25	−13·4		
1228	A	10	4	135	150	86·75	−12·8	62·87	12·98
1228	A	11	1	85	100	91·25	−13·5	71·09	15·16
1228	A	12	1	88	110	100·80	−10·8		
1228	A	14	1	135	150	111·80	−16·4		
1228	A	14	3	135	150	114·80	−17·6	73·83	20·09
1228	A	14	5	135	150	117·80	−17·9	76·98	21·15
1228	A	16	1	135	150	129·80	−16·4		
1228	A	16	3	135	150	132·80	−18·3		
1228	A	18	1	135	150	148·80	−16·4		
1228	A	18	3	135	150	151·80	−17·9		
1228	A	19	1	79	94	157·70	−17·2	90·88	28·22
1228	A	19	2	135	150	159·20	−19·6	94·48	29·54
1228	A	20	3	135	150	170·60	−17·1		
1228	A	21	1	135	150	177·30	−15·4		
1228	A	22	1	120	135	186·60	−15·6	80·77	26·62
1228	A	22	1	135	150	186·80	−16·2	96·92	32·04
1228	A	22	3	60	77	189·00	−16·5	94·26	31·17
1228	B	6	1	130	150	46·10		48·49	4·69
1228	B	6	4	130	150	50·60		56·01	6·99
1228	C	1	1	15	30	0·15		49·66	8·98
1228	C	1	1	30	45	0·30		53·32	8·19
1228	C	1	1	45	60	0·45		48·56	8·72
1228	C	1	1	60	75	0·60		48·05	8·62
1228	C	1	1	75	90	0·75		54·21	6·37
1228	C	1	1	90	105	0·90		49·29	8·53
1228	C	1	1	105	120	1·05		49·05	8·29

Table 3. Continued

Site	Hole	Core	Sect	Int. top (cm)	Int. bottom (cm)	Depth (mbsf)	$\delta^{13}C$ (‰PDB)	Mg^{2+} (mM)	Ca^{2+} (mM)
1228	C	1	1	120	135	1·20		49·14	6·87
1228	C	1	1	135	150	1·35		49·42	8·23
1228	E	1	1	12	25	0·12		48·73	9·23
1228	E	1	1	25	40	0·25		49·91	9·07
1228	E	1	3	100	115	4·50		49·98	5·04
1228	E	1	4	135	150	6·35		47·42	6·02
1229	A	1	1	135	150	1·35	−8·3	49·12	7·27
1229	A	1	3	131	148	4·31	−11·4	47·66	4·71
1229	A	2	1	135	150	6·25	−11·6	49·83	3·87
1229	A	2	5	135	150	12·25		44·59	4·60
1229	A	3	1	135	150	15·75	−11·4	45·16	7·34
1229	A	3	5	135	150	21·75	−11·5	43·59	7·05
1229	A	4	1	135	150	25·25	−14·2	42·27	6·78
1229	A	4	5	135	150	31·25	−14·6	41·19	2·78
1229	A	5	4	135	150	39·25	−7·9	44·05	6·60
1229	A	5	5	135	150	40·75	−9·5	42·82	7·45
1229	A	6	1	135	150	41·25	−10·5	42·29	7·62
1229	A	8	1	135	150	60·25	−6·1	50·97	9·23
1229	A	8	5	135	150	66·25	−7·0	50·49	9·24
1229	A	9	1	135	150	69·75	−6·4	53·57	11·54
1229	A	9	4	135	150	74·25	−9·8	54·21	11·40
1229	A	9	5	135	150	75·75	−9·7	52·96	10·80
1229	A	10	1	135	150	80·75	−8·4	54·97	11·59
1229	A	10	3	135	150	83·75	−12·7	55·46	11·48
1229	A	10	7	122	136	88·14	−10·4		
1229	A	11	1	135	150	90·25	−10·8		
1229	A	11	3	135	150	93·25	−12·3	61·87	13·01
1229	A	11	5	135	150	96·25	−14·2	62·62	13·95
1229	A	12	1	135	150	99·75	−15·2	64·16	14·55
1229	A	12	3	135	150	102·80	−14·5	67·24	15·81
1229	A	12	5	135	150	105·80	−14·3	65·61	16·09
1229	A	13	1	135	150	109·30	−14·4	71·46	8·93
1229	A	13	3	135	150	112·30	−14·3	68·82	10·48
1229	A	14	1	135	150	118·80	−14·6	74·06	11·07
1229	A	14	3	135	150	121·80	−11·8		
1229	A	15	1	49	64	127·40	−14·9		
1229	A	18	1	135	150	156·80	−14·8	90·65	17·33
1229	A	22	1	135	150	186·30	−15·9	105·80	21·93
1230	A	1	1	135	150	1·35	−10·4	48·27	5·08
1230	A	1	2	135	150	2·85	−11·9	46·72	4·38
1230	A	1	3	144	160	4·44	−12·0	49·31	3·97
1230	A	2	1	135	150	6·15	−12·6	48·28	3·05
1230	A	2	2	135	150	7·65	−13·2	48·18	2·66
1230	A	2	3	135	150	9·15	−8·4	50·30	2·50
1230	A	2	4	135	150	10·65	−6·2	50·41	3·94
1230	A	2	5	135	150	12·15	−3·4	48·98	3·59
1230	A	2	6	135	150	13·65	−0·9	52·06	3·68
1230	A	3	1	135	150	15·65	2·4	52·09	3·18
1230	A	3	2	135	150	17·15	4·0	53·72	3·45
1230	A	3	3	135	150	18·65	5·6	52·34	0·50
1230	A	3	4	135	150	20·15	6·4	56·09	3·45
1230	A	3	5	135	150	21·65	7·0	55·44	3·31
1230	A	3	6	135	150	23·15	7·8	56·93	3·44
1230	A	4	3	135	150	28·15	9·5	55·20	3·18
1230	A	4	5	135	150	31·15	10·4	55·44	3·16
1230	A	5	2	135	150	36·15	13·1	58·90	0·52
1230	A	5	5	135	150	40·65	13·1	60·79	1·59

Table 3. Continued

Site	Hole	Core	Sect	Int. top (cm)	Int. bottom (cm)	Depth (mbsf)	$\delta^{13}C$ (‰PDB)	Mg^{2+} (mM)	Ca^{2+} (mM)
1230	A	6	1	135	150	44·15		59·44	2·76
1230	A	6	3	143	158	47·23	14·0	57·60	2·61
1230	A	8	3	135	150	58·65	14·6	61·60	3·20
1230	A	8	5	135	150	61·65	15·0	60·34	3·24
1230	A	9	1	135	150	62·15	15·3	61·02	2·69
1230	A	9	6	135	150	68·25	15·9	60·43	2·78
1230	A	10	1	135	150	71·65	16·0	59·38	0·53
1230	A	10	5	135	150	77·65	16·3		
1230	A	11	1	135	150	81·15	16·6	60·89	3·53
1230	A	11	5	135	150	87·15	17·1	46·62	0·56
1230	A	12	2	135	150	92·15	17·1	58·35	1·05
1230	A	12	5	115	130	96·45	17·2	60·14	2·10
1230	A	13	1	135	150	100·15	17·7	60·09	0·39
1230	A	13	5	135	150	106·15	17·5	58·92	1·18
1230	A	14	1	135	150	109·65	17·3	60·61	1·16
1230	A	14	5	135	150	115·72	17·8	58·00	0·44
1230	A	15	2	135	150	119·47	17·5	58·07	3·61
1230	A	15	5	85	98	123·47	19·6	58·91	3·63
1230	A	15	7	135	150	126·89	18·4	52·78	0·26
1230	A	17	1	135	150	130·65	18·4		
1230	A	17	2	135	150	132·15	17·4	57·19	3·61
1230	A	18	1	130	150	140·10	17·5	55·50	3·25
1230	A	19	3	0	34	150·62	17·4	52·17	3·03
1230	A	21	3	135	150	161·63	17·3	54·78	3·86
1230	A	22	1	75	90	169·05	18·2	51·78	3·86
1230	A	24	1	135	150	188·65	16·3	51·10	4·23
1230	A	26	2	14	28	199·91		39·96	3·37
1230	A	35	1	136	156	246·36	15·1	35·98	2·43
1230	A	38	2	0	19	268·70		36·69	6·33

seawater Sr isotope composition compiled by Veizer *et al.* (1999) was used for comparison.

Mg and Ca concentrations (Table 3) were measured with a high-resolution sector field inductively coupled plasma mass spectrometer (ICP-MS, Finnegan Element2 – Thermo Fisher Scientific Inc., MA, USA) at Woods Hole Oceanographic Institution. Instrumental precision for Mg/Ca, based on repeated measurements of a series of standards, is 0·03 mmol mol^{-1}.

Numeric diffusion model

Sulphate porewater profiles were simulated using a transient diffusion model including a sink term, i.e.:

$$\frac{\partial c}{\partial t} = \kappa \frac{\partial^2 c}{\partial x^2} + s(x) \qquad (1)$$

where $c(x,t)$ is the concentration of sulphate (mM), t is time (a), and x is the depth below seafloor (mbsf).

$$\kappa = \phi \tau^{-2} D_s \text{ and } \tau^2 = \phi F$$

where D_s is the diffusion coefficient for sulphate ($m^2\ s^{-1}$), ϕ is the porosity (dimensionless), F is the formation factor (dimensionless) and the sulphate reduction rate $s(x)$ is:

$$s(x) = \begin{cases} 0 \text{ mmol m}^{-3} \text{ a}^{-1} \\ \text{if } t < 10000 \text{ a} \\ -50 \text{ mmol m}^{-3} \text{ a}^{-1} \\ \text{if } 10000 \text{ a} < t < 11400 \text{ a and } 2.5 < x < 5 \text{ mbsf} \end{cases}$$

The following initial conditions and boundary conditions were used:

$$c = \begin{cases} 0 \text{ mM} & \text{for } x > 0 \\ 28 \text{ mM} & \text{for } x = 0 \end{cases}$$

$$c(0, t) = 28 \text{ mM}$$

$$c(L, t) = 0 \text{ mM}$$

where L is the length of the model domain.

Eq. (1) was solved using an explicit finite difference method with a time step of 10 years and a grid size of 0·5 m. A factor for tortuosity was considered, which was calculated from porosity and formation factor (Boudreau, 1997). Typical values of the formation factor F (3) (from electrical resistivity measurements) for Site 1229 and a diffusion coefficient of 7·86 E−10 m^2 s^{-1}, given in Schulz & Zabel (2000) for sulphate at 15 °C, were used. Note that $s(x) = 0$ for the first 10 000 years of the computation, which is the time required for sulphate to diffuse to the present sulphate–methane interface at approximately 30 mbsf. Once this is achieved, sulphate reduction is switched on in the depth interval $2{\cdot}5<x<5$ m to simulate the effect of strong sulphate reduction in an organic carbon-rich sediment layer. Sulphate reduction with a rate of 50 mmol m^{-3} a^{-1} (which is at the upper limit of values typical for deep-sea sediments; Schulz & Zabel, 2000) was assumed in a horizon from 2·5 to 5 mbsf.

RESULTS

Petrography

The petrography of dolomite recovered during ODP Leg 201 on the Peru Margin is described in detail in Meister *et al.* (2006). All dolomite samples show well-ordered crystal symmetry with $CaCO_3$ compositions of 50 to 56 mol% (Meister *et al.*, 2006). Dolomite was recovered as discrete layers or fragments within nearly carbonate-free unlithified diatomaceous and siliciclastic sediment at the outer shelf and upper slope of the Peru Margin (Fig. 2A) and in one sample from 7 mbsf in the Peru Trench (ODP Leg 112, Site 685). Dolomite layers are most abundant at Site 1229 and their distribution correlates in general with the occurrence of organic carbon-rich sediments. This observation is supported by the correlation of dolomite layers with the colour reflectance (Fig. 3), which can serve as a proxy for total organic carbon (TOC) content. The TOC (Meister *et al.*, 2005) and colour reflectance both correlate with the bathymetry reconstructed from benthic foraminiferal assemblages (Resig, 1990), as shown in Fig. 3. Based on this correlation, dolomite layers are associated with organic carbon-rich, highstand sediments. However, dolomite layers can occur in both diatomaceous and siliciclastic sediment (Fig. 4A and B) and are, thus, not directly related to a specific lithology.

Dolomite layers are usually dense, fine-grained and well lithified. Friable dolomite occurs as laminae only associated with hard layers and disseminated dolomite is unevenly distributed throughout the recovered Leg 201 drill cores. The lithified layers often show parallel and non-concentric lamination and the recovered pieces probably represent fragments of extended lenses or layers that were broken by piston coring. This type of dolomite is similar to the layers and lenses found in the diatomites of the Miocene Monterey Formation (California), which often extend laterally to hundreds of metres (Fig. 2B and C). ODP Leg 201 dolomite layers show variable thicknesses at different sites, but, within each site, thicknesses remain relatively constant. Petrographic relationships indicate a primary precipitation with no replacement of precursor carbonate (Fig. 5; Meister *et al.*, 2006). Dolomite cement consists of euhedral decimicron-size rhombs, which enclose and replicate fresh surfaces of diatom frustules (Figs 4A and 5A) and foraminiferal tests (Fig. 5B and C). Cathode luminescence (Fig. 4C–E) reveals the dolomite phase clearly growing after the precipitation of fibrous calcite cements, which occur in the cavities of some of the foraminiferal tests. Framboidal pyrite was often found growing in the gaps between dolomite rhombs and, therefore, post-dates the precipitation of the dolomite (Fig. 5D).

Carbon and oxygen isotopes

Carbon isotope ratios measured in the Peru Margin dolomites ($\delta^{13}C_{DOL}$) are highly variable (Figs 6 and 7; Table 1), whereas $\delta^{18}O_{DOL}$ values fall into a narrow range with an average value of $3{\cdot}50 \pm 1{\cdot}15‰$, which reflects possible isotopic equilibrium with porewater or seawater composition. The $\delta^{13}C_{DOL}$ values range from −15 to +15‰ PDB at the shelf sites (Sites 1227/684, 1228/680 and 1229/681; Fig. 7A–C). After the classic concept (Claypool & Kaplan, 1974), this wide range from negative to positive values indicates sulphate reduction or methanogenic activity, respectively, at the time of precipitation. Additionally, values ranging from −25‰ to −36‰ were measured in the dolomite layer at 7 mbsf at the trench site (ODP Leg 112, Site 685), which provides strong evidence for methane oxidation (Fig. 7D). Significant variations occur often within particular sites, such as Site 1229/681, where two positive $\delta^{13}C_{DOL}$ spikes of +6‰ occur around 40 and 100 mbsf. In general, $\delta^{13}C_{DOL}$ profiles do not reflect recent

Fig. 2. Petrography of the Peru Margin dolomites. (A) Fragment of discrete dolomite layer in ODP Leg 201 drill core (Sample 201-1228B-6H-2; 47·2 mbsf), which occurs as fine-grained, hard-lithified fragments broken by the drilling process. Parallel lamination is often observed, but no concentric lamination occurs (cm scale bar). (B) Dolomite layer (arrow) in porcellanite of the Miocene Monterey Formation, Arroyo Seco, CA, which probably represents the fossil analogue of the Peru Margin dolomites. (C) Close up photograph of the same dolomite layer (approximately 10 cm thick) (B) showing parallel lamination; car key for scale. (See further descriptions in Meister *et al.*, 2006.)

microbial activity at different depths and often dolomite with positive $\delta^{13}C_{DOL}$ values occurs in zones where modern porewater chemistry indicates sulphate reduction, and negative values were measured in dolomites recovered from the modern methanogenic zone.

Carbon isotope values measured in dissolved inorganic carbon ($\delta^{13}C_{DIC}$) in the porewater (Fig. 7, Table 3) commonly are consistent with the porewater chemistry, i.e. $\delta^{13}C_{DIC}$ values range from −20 to −10‰ in the sulphate reduction zone and increase in the methanogenic zone. Absolute values in the methanogenic zone, however, show a broad range from −7‰ at Site 1229 to +17‰ at Site 1230. This pattern matches the recent microbial activity with relatively low CH_4 production in a 50 m thick methanogenic zone at Site 1229 and strong methanogenic activity with gas hydrate formation at Site 1230. Only a gradual transition in

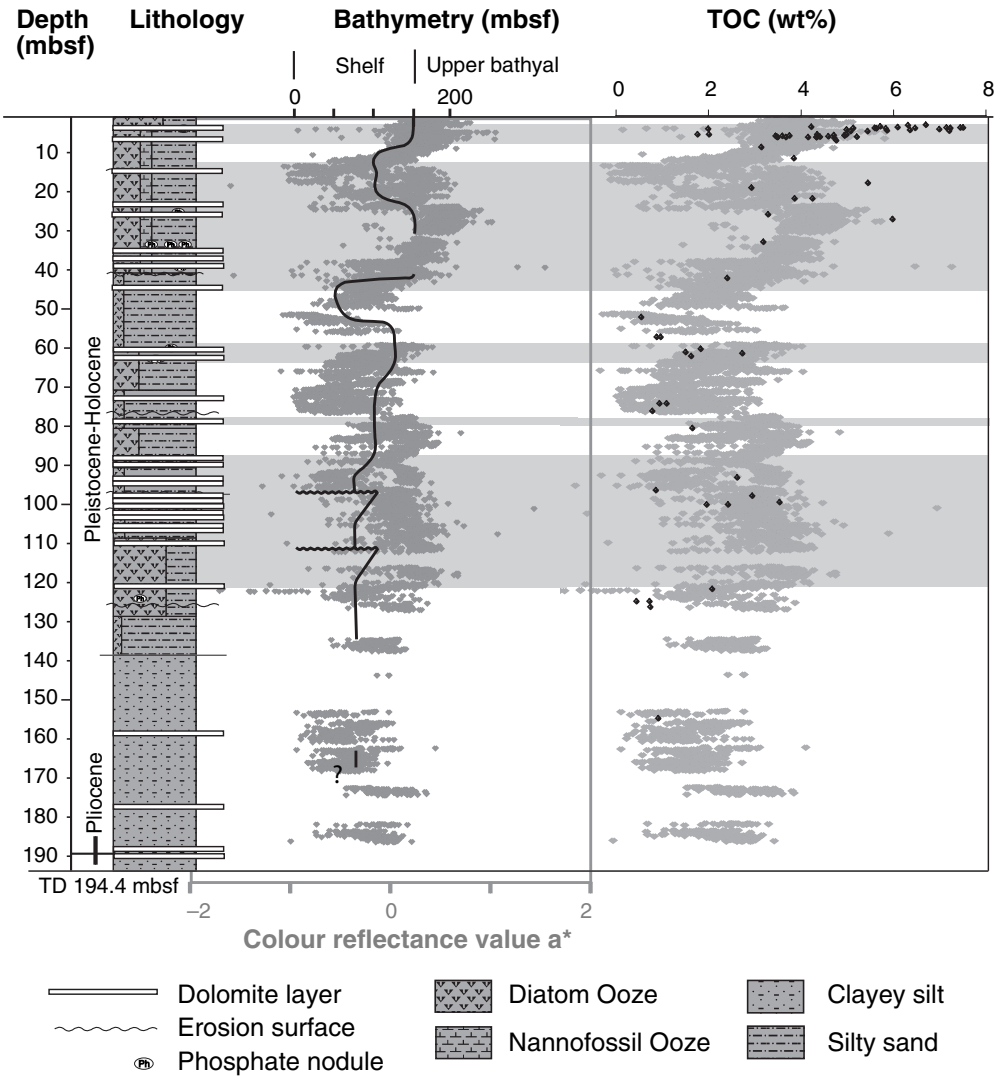

Fig. 3. Correlation of frequency of dolomite layers with TOC content (black diamonds; Meister *et al.*, 2005) at shelf Site 1229. TOC-rich horizons can be correlated with higher colour reflectance (a^*) values (shaded diamonds; D'Hondt *et al.*, 2003) and palaeobathymetry (black line) reconstructed from benthic foraminifera (Resig, 1990). Periodic fluctuations of TOC and colour reflectance data have been related to glacial-interglacial cycles (Wefer *et al.*, 1990).

$\delta^{13}C_{DIC}$ from −15‰ to −7‰ is present at the SMI at Site 1229, whereas a negative spike in $\delta^{13}C_{DIC}$ occurs at the SMI at Site 1230, which is probably due to AMO. Both, $\delta^{13}C_{DIC}$ and relatively low CH_4 concentrations indicate that AMO is probably a minor process at the shelf sites, even if evidence for high microbial activity at the SMI was found (D'Hondt *et al.*, 2003).

Although, in general, $\delta^{13}C_{DIC}$ is in equilibrium with the modern redox zonation, $\delta^{13}C_{DIC}$ at Site 1227 shows a different pattern in two different drill holes. In fact, the minimum in $\delta^{13}C_{DIC}$ occurs 20 m above the modern SMI and the $\delta^{13}C_{DIC}$ values scatter between −15 and +2‰ at the SMI. This pattern does not reflect recent microbial activity and may be due to a non-steady-state situation. Also, the minimum in $\delta^{13}C_{DIC}$ at Site 1230 occurs a few metres above the modern SMI.

In summary, the $\delta^{13}C_{DOL}$ values are not in equilibrium with the modern porewater $\delta^{13}C_{DIC}$. Even the signal for AMO measured in the dolomite sample at the trench site (−33‰, Fig. 7D) is not reflected in $\delta^{13}C_{DIC}$.

Strontium isotopes

Strontium isotope ratios measured in dolomite ($^{87}Sr/^{86}Sr_{DOL}$) are plotted against depth in Fig. 8. These ratios vary at the shelf sites (Sites 1227,

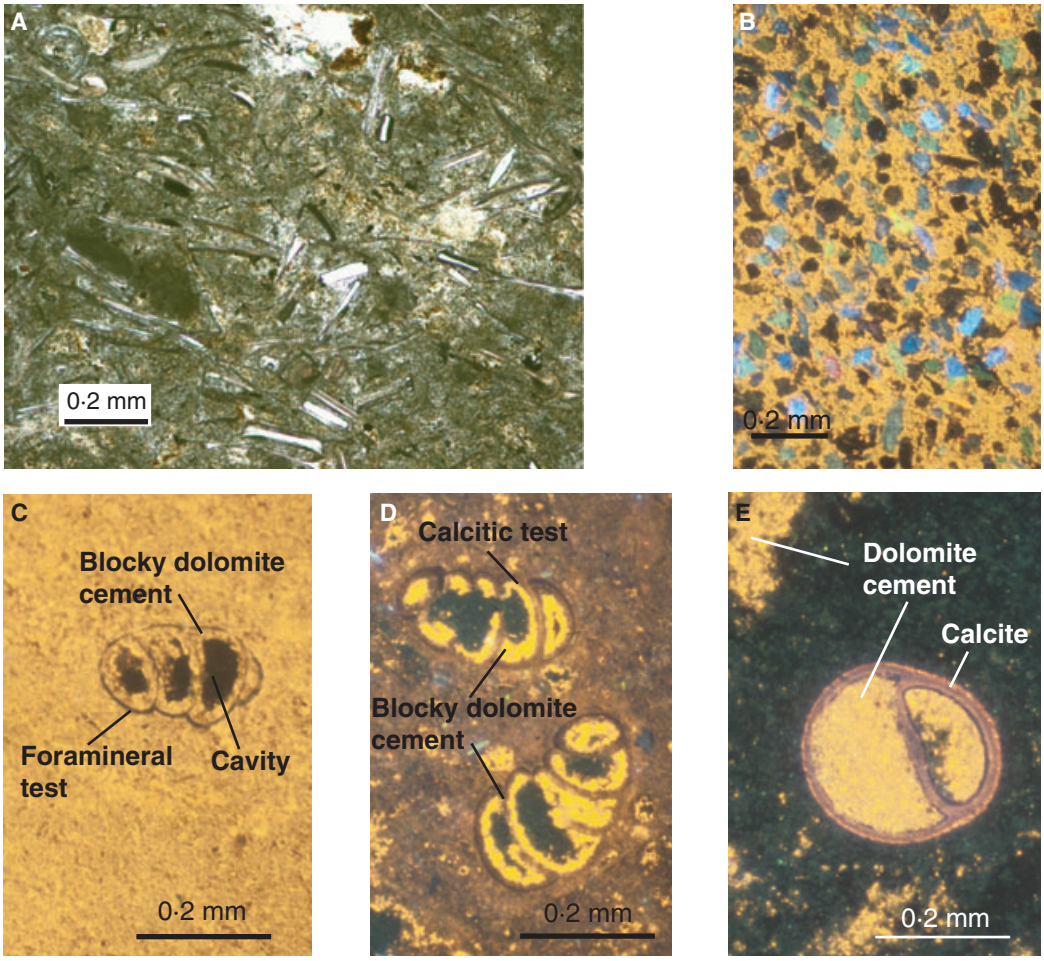

Fig. 4. Photomicrograph and cathodoluminescence images of Peru Margin dolomite layers. (A) Diatom frustules are cemented by densely lithified euhedral dolomicrosparite with grain sizes of approximately 10 μm (Sample 201-1229A-10H-1, 133 to 136 cm; 80·7 mbsf). (B) 10 μm size angular quartz fragments cemented by dolomicrosparite (Sample 201-1229A-8H-1, 55 to 64 cm; 59·5 mbsf). (C) Cathodoluminescence of foraminiferal test in highly luminescent dolomicrosparite. The tests show growth of blocky dolomite cement rim surrounding the central cavities (Sample 201-1229A-4H-2, 95 to 96 cm; 26·3 mbsf). (D) Cathodoluminescence image of foraminiferal tests in fine-grained mudstone-dolomicrosparite matrix. The calcitic test shows reddish colour due to calcite staining. Locally, the tests show growth of thin seams of fibrous calcite cement. The central cavities have a rim of blocky, strongly luminescent dolomite cement (Sample 201-1229A-12H-2, 86 to 88 cm; 100·8 mbsf). (E) Similar to sample (C) and (D), but central cavity is entirely filled with dolomite cement.

1228 and 1229; Fig. 8A–C) between 0·7086 and 0·7093, which is near to seawater composition or composition of the porewater present in the uppermost 30 mbsf. One value at Site 1228 (0·70928) is slightly more radiogenic than modern seawater; this may be due to a leaching effect (Na-acetate buffer was used for this sample) or may be a local diagenetic effect (e.g. leaching of volcanic ash).

Porewater Sr isotope values ($^{87}Sr/^{86}Sr_W$) correlate with the data of Kastner *et al.* (1990); Fig. 8C). In general, $^{87}Sr/^{86}Sr_W$ strongly deviates from the seawater composition. The Peru shelf sites show decreasing $^{87}Sr/^{86}Sr_W$ with depth, which is due to diffusive mixing of seawater and brine Sr. At Site 1229, a nearly linear depth gradient has been established between seawater (0·7091) and brine (<0·7080; Fig. 8C). In contrast to the high vertical gradient observed in the porewater $^{87}Sr/^{86}Sr_W$, seawater values (Veizer *et al.*, 1999) have only slightly changed during the Pleistocene (Fig. 8A–C), and the Sr concentration increases from 100 μM at the sediment–water interface to 350 μM in the brine. Comparison of the brine $^{87}Sr/^{86}Sr$ values with the reconstructed seawater values shows that the brine may have formed earlier than the Miocene. The low Sr isotope composition of the brine could also be explained by silicate diagenesis of volcanic ash layers. However, the ash

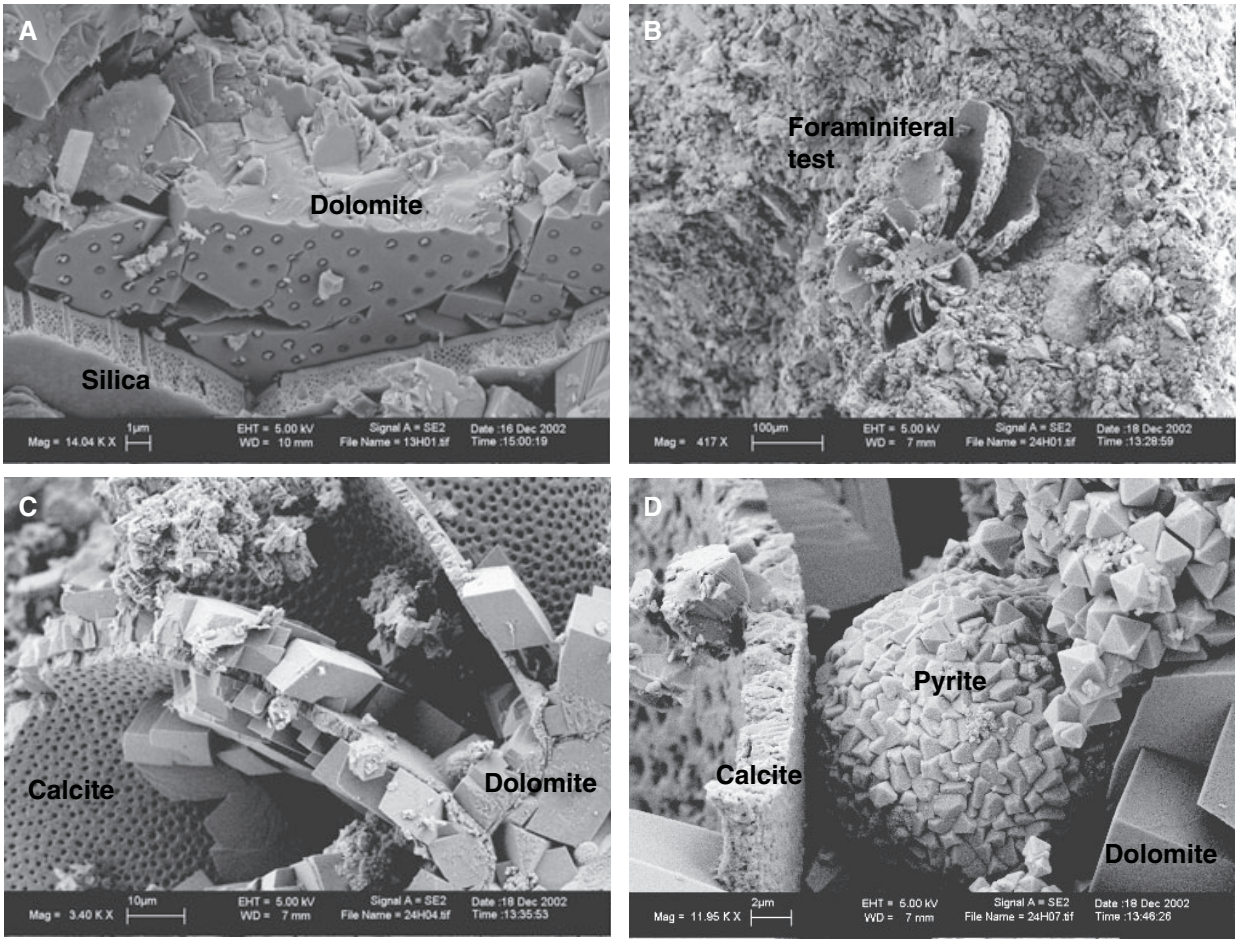

Fig. 5. Scanning electron microscopy images of Peru Margin dolomite layers: (A) Well-preserved diatom frustule (bottom) with replica structures on dolomite crystal (centre) (Sample 201-1228A-6H-6, 62 to 70 cm; 51·2 mbsf). (B) Decimicron-scale dolomite rhombs growing on the surface of a perforate foraminiferal test. Precursor calcite was not dissolved by this process (Sample 201-1229A-8H-1, 55 to 64 cm; 59·5 mbsf). (C) Details of (B). (D) Details of (C) showing framboidal pyrite growing in the empty pore space between dolomite rhombs. Pyrite precipitation, thus, post-dates the formation of dolomite.

layers described from Leg 201 (Hart & Miller, 2006) are predominantly K-rich, which would produce a more radiogenic signal. The few more radiogenic values at Site 1228 may be explained by leaching of ashes but the composition of the brine is probably due to old seawater. Sr isotopic values of porewater at the trench site (Site 1230) follow precisely the Sr-composition of the seawater above 150 mbsf but increase continuously to 0·710 below that depth, which is probably related to an inflow of hydrothermal fluid (data not shown).

Mg and Ca concentrations and carbonate alkalinity

Magnesium and calcium concentrations generally decrease up to 10 mM relative to the seawater concentration in the uppermost 30 mbsf at the shelf sites, reaching a minimum before rising continuously to 110 and 35 mM respectively (Fig. 9A–C). This increase is caused by the upward diffusion of Mg and Ca from the brine, which is present at greater depth at the shelf sites. At the trench site (Site 1230), no increase is recorded at depth (Fig. 9D). However, an increase of Mg to 60 mM at 40 mbsf was measured which cannot be explained by the presence of an enriched fluid. Nevertheless, a local sink is indicated by a change in slope around 8 mbsf, which correlates with the minimum in Ca concentration. On a broad scale, at most sites, minima in Mg and Ca occur in the depth range of the SMI, with additional (minor) minima close to the sediment surface. Only Site 1227 seems to show a somewhat more pro-

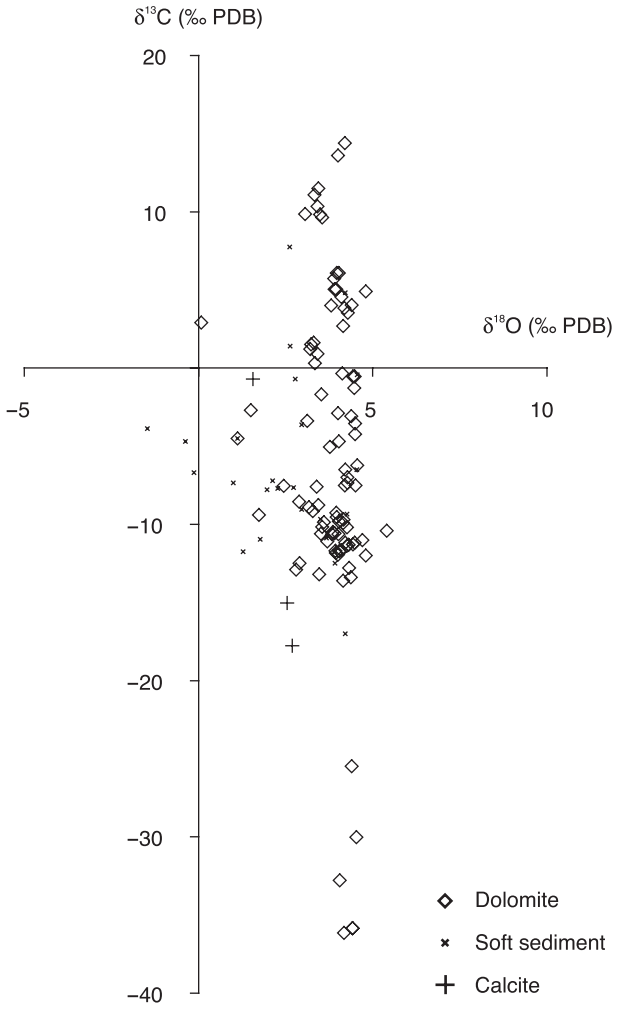

Fig. 6. Cross-plot of $\delta^{13}C_{DOL}$ vs. $\delta^{18}O_{DOL}$ of dolomite layers recovered from ODP Leg 201 and 112 drill sites. Data from Thornburg & Suess (1990) measured in the micrite are included in the plot. Whereas $\delta^{18}O_{DOL}$ values are generally close to isotopic equilibrium with porewater of seawater origin, the $\delta^{13}C_{DOL}$ values are strongly variable ranging from −37‰ to +15‰. These variations may reflect highly variable conditions in the deep-sea hemipelagic diagenetic system through time.

nounced minimum near 10 mbsf than at the SMI near 40 mbsf.

Minima in Mg and Ca concentrations correlate with maxima in carbonate alkalinity (Fig. 9). These alkalinity maxima occur mostly at the SMI, where alkalinity is produced by strong microbial degradation of organic matter. Also, alkalinity maxima occur at a very shallow depth at Sites 1228 and 1229, which are correlated with the less pronounced minima in Mg and Ca. At Site 1227, a change in slope occurs in the alkalinity profile at 10 mbsf, which correlates with the lowest concentrations in Mg and Ca. At all shelf sites, alkalinity is decreasing below the SMI, which is due to the brine, but also indicates relatively low microbial activity in the methanogenic zone and the lower sulphate reduction zone. At the trench site (Fig. 9D), where no brine is present, alkalinity is further increasing in the methanogenic zone, however, with a less steep gradient; this indicates a net production of alkalinity at the SMI. Nevertheless, alkalinity of 150 mM around 100 mbsf was the highest of all studied sites.

Sulphate diffusion model

Sulphate concentration profiles measured by shipboard analysis (D'Hondt *et al.*, 2003) were simulated using a numeric diffusion model (Fig. 10A). As starting conditions, a seawater sulphate concentration of 28 mM was used with no sulphate in sediment porewater. The model calculated the concentration as a function of time and depth. After 10 000 years, sulphate had diffused downwards to 30 mbsf. The model also shows that, assuming a surface layer with a sulphate reduction rate of 50 mmol m^{-3} a^{-1} in a 2·5 m thick interval at 2·5 to 5 mbsf, the SO_4^{2-} in this zone will be consumed within a time period of 1000 years. Moreover, the profile returns to its original shape within another 1000 years as soon as consumption ceases. The model reproduces the porewater SO_4^{2-} profile measured in the natural environment at Site 1229 (Fig. 10B). The effect of advection is probably minor in this setting, which is indicated by the linear Cl^- concentration profile. For the same reason, variations in porosity are probably less important than the variation in TOC.

DISCUSSION

Depth of dolomite formation

The $^{87}Sr/^{86}Sr$ ratios of all of the studied dolomite plots close to the profile for Quaternary seawater composition (Fig. 8) indicate that all of the samples have an early diagenetic origin and have not precipitated from hydrothermal fluids. Additional evidence from petrographic relationships indicates primary precipitation of dolomite in the sedimentary sequence of the upper slope and outer shelf sites with cementation and no replacement of precursor carbonate. The growth of framboidal pyrite post-dates the precipitation of the dolomite, providing additional support for early dolomite formation. At all sites, HS^- con-

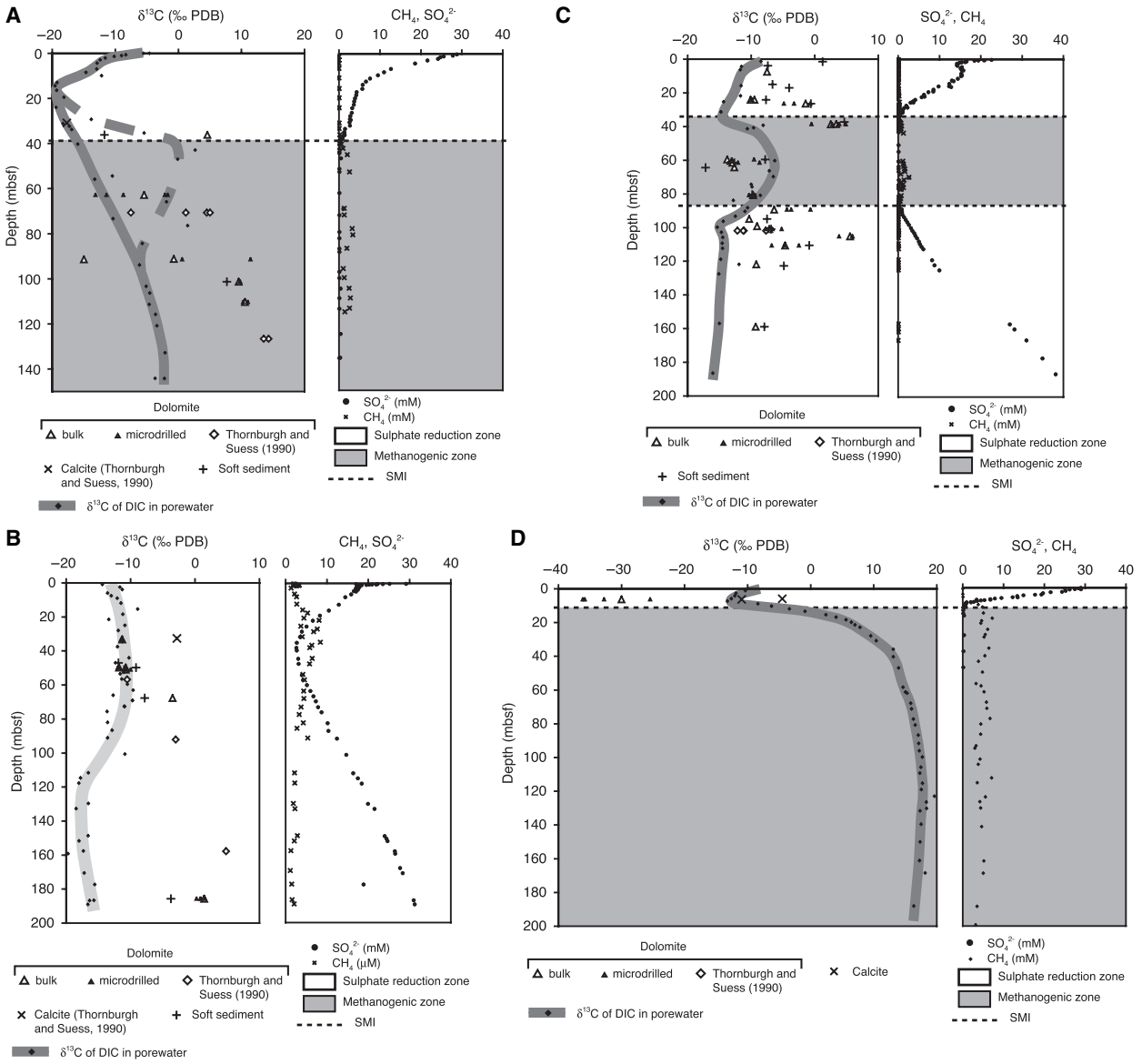

Fig. 7. Carbon isotopic composition (‰PDB) of dolomite, calcite, soft sediment and porewater from (A) Site 1227/684, (B) Site 1228/680, (C) Site 1229/681 and (D) Site 1230/685 respectively. Values measured by Thornburg & Suess (1990) in the carbonates are included in the plots. Comparison with sulphate and methane concentration profiles measured in the porewater (D'Hondt *et al.*, 2003) shows that $\delta^{13}C_{DIC}$ reaches values between −10 and −20‰ in the sulphate zone. At all sites, although the $\delta^{13}C_{DIC}$ is elevated in the methanogenic zones, the values may still be negative (e.g. Site 1229). $\delta^{13}C_{DOL}$ values in dolomite layers are, in general, not in isotopic equilibrium with the modern porewater. (Shaded area indicates methanogenic zone, unshaded area indicates sulphate reduction zone, dashed line indicates SMI).

centrations decrease below the SMI, often reaching 0. Below this depth, Fe^{2+} is remobilized and available to nucleate as framboidal crystals. Dissolved iron has been measured in the methanogenic zone by shipboard analysis but is below the detection limit in the sulphidic zone (D'Hondt *et al.*, 2003). Early formation of dolomite layers has been reported from other deep-sea sites, such as the Romanche Fracture Zone in the equatorial Atlantic (Bernoulli *et al.*, 2004) and in the Oligocene to Miocene deep-sea fan succession of the Gonfolite Lombarda Group, northern Italy (Bernoulli & Gunzenhauser, 2001).

Strontium isotope and carbon isotope data indicate a general disequilibrium between dolomite and modern porewater. Also, $\delta^{18}O$ values around 4‰ are within the range expected for dolomite precipitated from seawater under low-

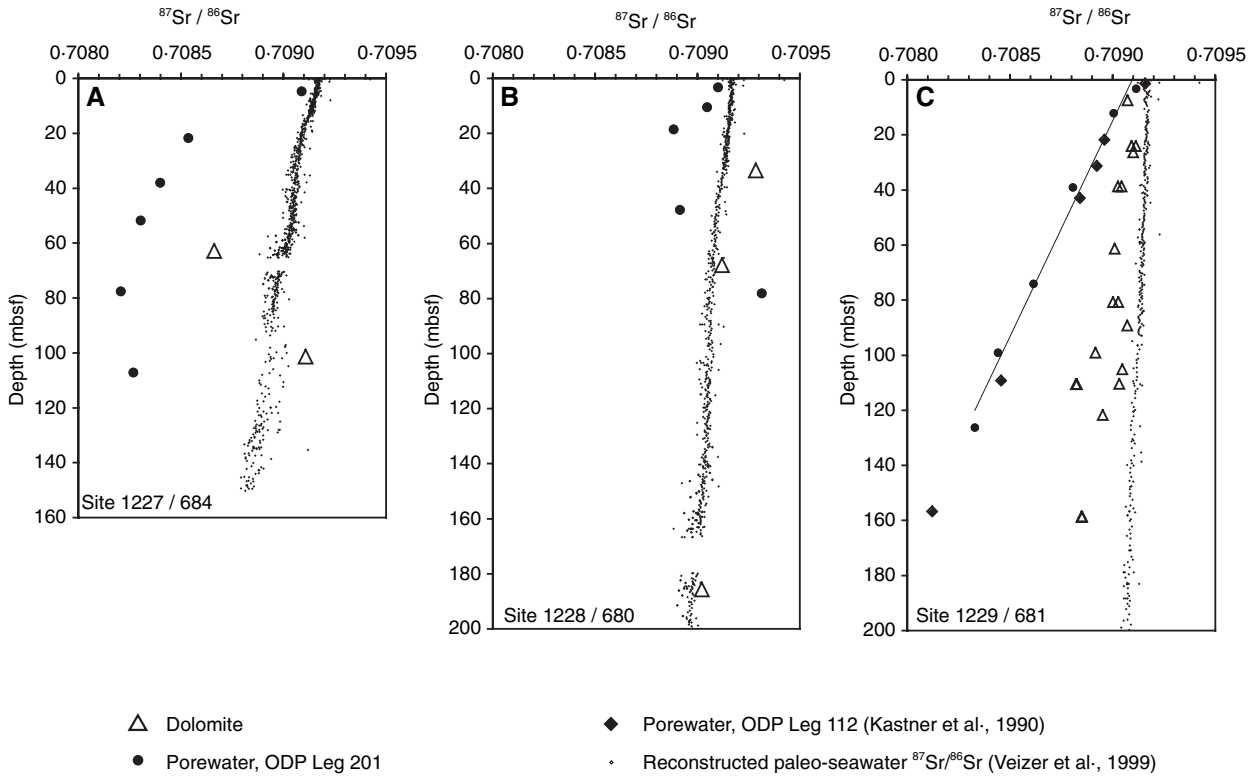

Fig. 8. Sr isotopic compositions of dolomite, porewater (Kastner *et al.*, 1990; this study) and reconstructed seawater (Veizer *et al.*, 1999) plotted vs. depth at (A) Site 1227/684, (B) Site 1228/680 and (C) Site 1229/681. Dolomite layers from the shelf sites show $^{87}Sr/^{86}Sr$ values near surface porewater composition, whereas porewater $^{87}Sr/^{86}Sr$ values are generally decreasing with depth reaching 0·7081 at Site 1229.

temperature conditions (Vasconcelos *et al.*, 2005). Some scatter in the data is probably due to varying seawater composition and palaeotemperatures throughout the Quaternary. These disequilibria suggest that the dolomite formation occurred mainly in the past, and the depth of present dolomite formation is reflected primarily in the porewater chemistry. Since the $^{87}Sr/^{86}Sr$ values in the porewater show a linear gradient, due to diffusive mixing between brine and seawater, the vertical projection of the values measured in the dolomites on the mixing line (regression line at Site 1229) constrain dolomite precipitation to the uppermost 30 mbsf within the sequence at the Peru Margin shelf Site 1229/681 (Fig. 8C). Also, Sites 1227/684 (Fig. 8A), and 1228/680 (Fig. 8B) show similar trends, with a few more radiogenic values at Site 1228/680. Even if these values are due to leaching of volcanic ash layers of a different composition (see Hart & Miller, 2006), the disequilibrium between $^{87}Sr/^{86}Sr_{DOL}$ and $^{87}Sr/^{86}Sr_{W}$ still indicates that the dolomite layers form at shallow depth. Layers that occur at greater depths than 30 mbsf are not forming now but formed in the past, when they where located nearer to the sediment/water interface. Thus, the $\delta^{13}C_{DOL}$ values can be used as a proxy for the activity of the 'deep biosphere' in the past (see below).

Porewater Mg and Ca profiles show the most pronounced concentration minima around 30 mbsf and indicate that present dolomite formation probably occurs at this depth (e.g. Site 1229; Fig. 11C). Therefore, downward diffusion from seawater, as well as upward diffusion from the brine delivers Mg and Ca for dolomite formation. To form a dolomite layer of 3 to 5 cm thickness, precipitation must be focused at a particular site with Mg and Ca diffusing to that site for a certain amount of time. In fact, with the Mg-gradients commonly observed at the studied sites, a dolomite layer in the range of 2 to 3 mm per 10 000 years would be precipitated. These are minimum rates not taking into account the episodicity of the dolomite formation, but it is consistent with the amount of dolomite formed throughout the Quaternary. The minima of the Ca and Mg correlate with maxima in alkalinity, where alkalinity is highly increased by sulphate reduction. Elevated alkalinity in the uppermost 5 mbsf is probably due to sulphate-reducing

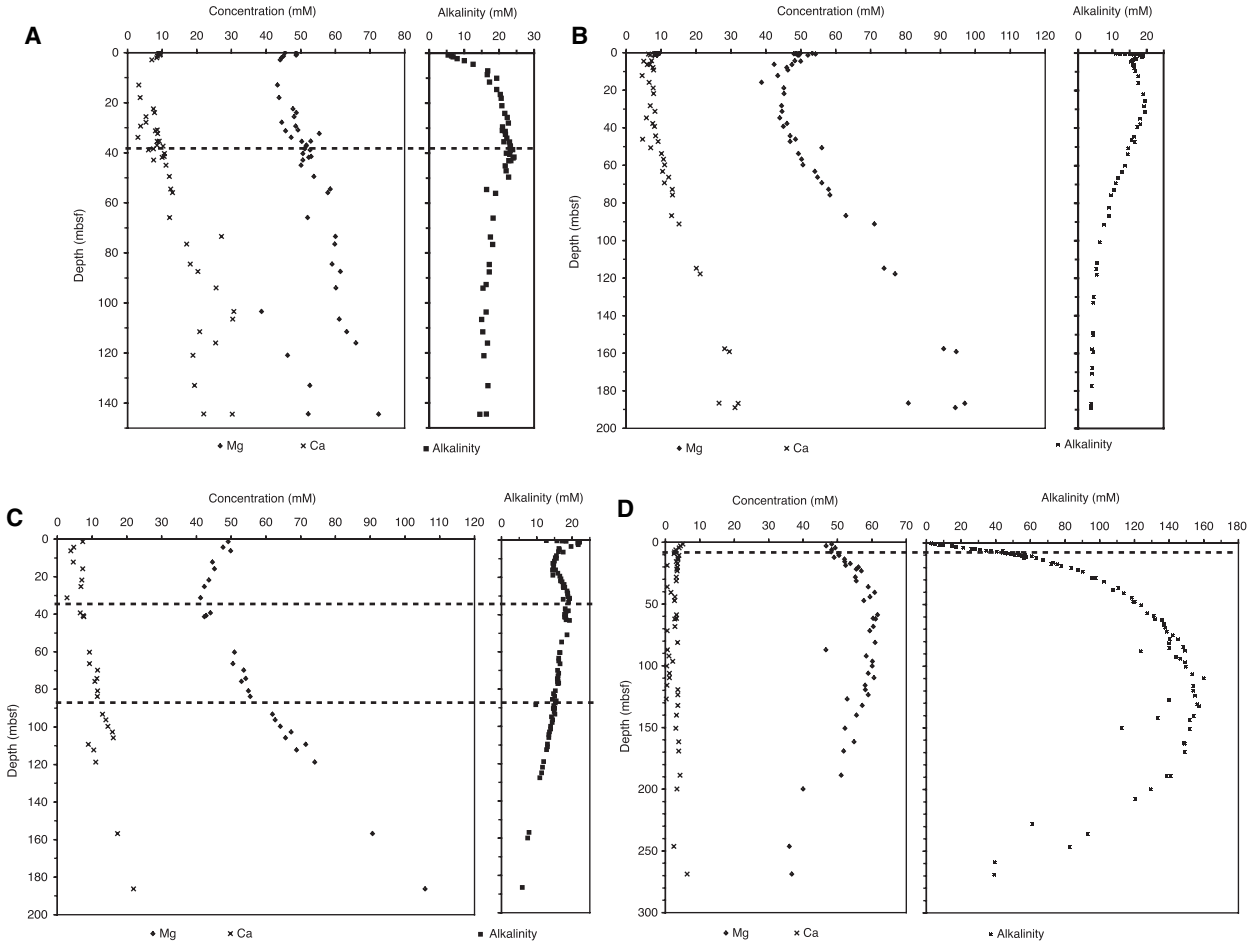

Fig. 9. Alkalinity, Mg, and Ca concentrations in porewater from (A) Site 1227, (B) Site 1228, (C) Site 1229 and (D) Site 1230 respectively. In general, alkalinity profiles show the mirror image of the Mg and Ca profiles, except for Site 1230, where Mg is unusually high in the uppermost 200 mbsf. Maxima in alkalinity and minima in dissolved Mg and Ca concentrations generally occur in the uppermost 30 mbsf and in particular coincide with the SMI.

activity in freshly deposited organic carbon-rich layers, whereas the high alkalinity at 30 mbsf is due to increased microbial activity at the SMI. At Site 1227, alkalinity at 5 mbsf is higher than at the SMI and correlates with the Mg and Ca profiles, which show a pronounced minimum at this depth. It is also noted that at Site 1227 there is evidence that the modern porewater chemistry is not in equilibrium with the current redox zonation and that the SMI has shifted downwards in the recent past. In summary, based on the interpretation of the data, active dolomite formation is restricted to the most biogeochemically active horizons, which is often coincident with the SMI.

The microbial factor in dolomite precipitation

In the classic concept, the depth and the diagenetic zone of formation are controlled by the sedimentation rate, which limits the downward diffusion of SO_4^{2-} from seawater (Kelts & McKenzie, 1984; Baker & Burns, 1985; Burns & Baker, 1987). Depending on the depth of diffusion, dolomite is formed either in the sulphate reduction zone or in the methanogenic zone and shows the $\delta^{13}C$ values typical for the zone of formation (Claypool & Kaplan, 1974). In this 'organic dolomite model', the depth of major organic matter degradation is, therefore, determining where dolomite precipitates independent of the biological activity at the site of precipitation.

In general, our interpretation is in agreement with this model, however, it is suggested that the formation of distinctive layers occurs at strictly focused sites within the sedimentary section, along geochemical interfaces, where the microbial activity is the driving force for dolomite precipitation. The observation of 'microbial hotspots' coincident with the SMI (Fig. 11), maxima

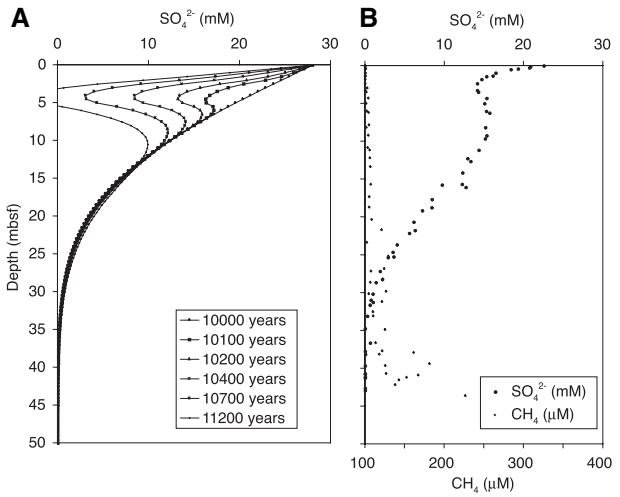

Fig. 10. (A) Solution of a numeric model simulating non-steady state sulphate concentrations in porewater affected by diffusion and consumption. Using a sulphate reduction rate of 50 mmol m^{-3} a^{-1} in a 2·5 m thick interval at 2·5 to 5 mbsf, sulphate can be rapidly consumed (within 1000 years). This produces a temporary sulphate reduction zone in the near surface sediments tens of metres above the modern sulphate–methane interface (SMI). With the constant consumption of organic matter, the sulphate concentration curve will return in a relatively short time (a few 1000 years) to its original shape, showing a gradual decrease in sulphate with depth to the SMI. (B) The porewater sulphate profile of Site 1229 shows the presence of a similar S-shaped curve in the uppermost 10 mbsf, as produced by the model run.

in alkalinity and minima in Mg and Ca concentration support this hypothesis and would explain the focused growth of multiple, less than 5 cm thick, dolomite layers within a more than 100 m thick sedimentary succession with diffusion of Mg and Ca over long distances towards that particular site independent of the lithology at the particular horizon. Based on the different models used to explain dolomite formation, the biogeochemical activity found at the SMI would, in any case, favour dolomite precipitation. Alkalinity is strongly increased at the SMI, which increases the supersaturation of dolomite at this particular horizon. Often, the SMI shows maxima in alkalinity or a sharp change in slope (e.g. Site 1230), which indicates net production of alkalinity. As a secondary effect, by the consumption of Mg and Ca in stoichiometric proportions during dolomite precipitation, the Mg/Ca ratio is increased. Kinetically, dolomite precipitation may be favoured by eliminating the inhibiting effect of SO_4^{2-}, as suggested by Baker & Kastner (1981). However, this effect has not been demonstrated for low-temperature conditions. Most importantly, the SMI shows extraordinarily high cell concentrations (Fig. 10; D'Hondt *et al.*, 2003, 2004; Parkes *et al.*, 2005) and can be considered as a microbial 'hotspot' within a deep sub-seafloor biosphere. The presence of living microbes is required for low-temperature dolomite precipitation, as shown by van Lith *et al.* (2003), by

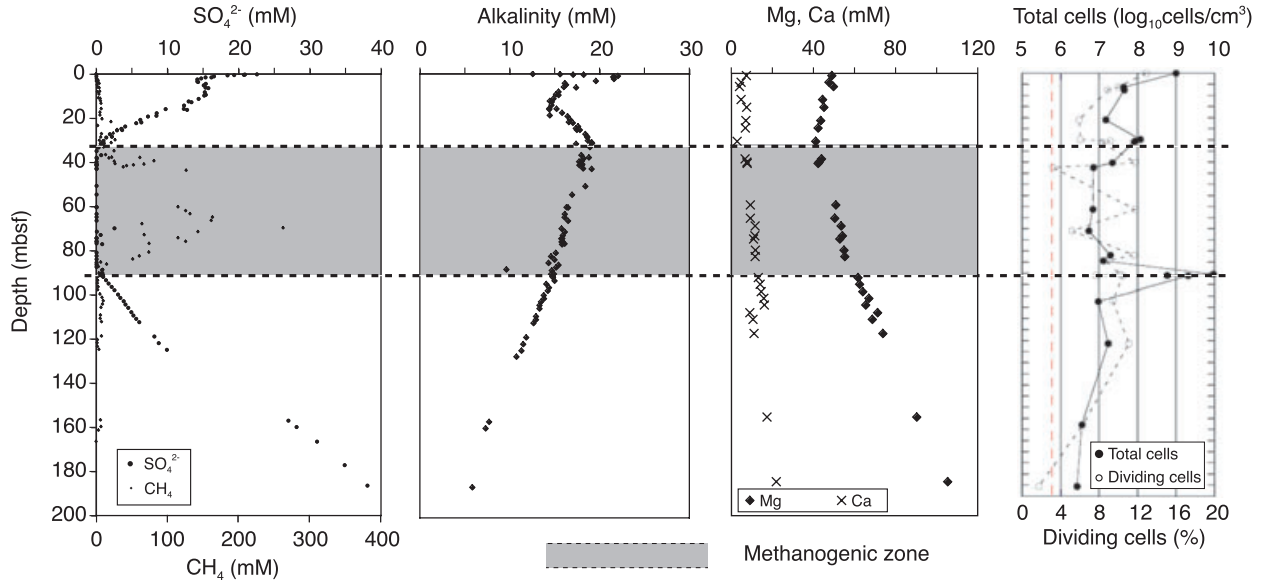

Fig. 11. Correlation of sulphate and methane concentration with alkalinity, Mg and Ca concentrations and bacterial cell counts at Site 1229 (D'Hondt *et al.*, 2003), showing high cell concentrations at the upper and lower SMIs. At these boundaries increased microbial activity occurs, which causes maximum alkalinity at these depths with the potential to induce dolomite precipitation.

providing the appropriate physico-chemical conditions to overcome the kinetic inhibition. The mechanism of this mediation process is not clearly understood and needs to be investigated. Possibly, the formation of extracellular polymeric substances (EPS) along geochemical interfaces may play an important role, but remains to be observed in deep-sea sediments. A similar interpretation was based on observations from a Bahamian stromatolite, where calcite crystals formed in a single EPS layer attributed to high sulphate reducing activity (Visscher *et al.*, 2000).

The type of microbial activity at the present SMI is indicated by $\delta^{13}C_{DIC}$, which often reaches strongly negative values due to AMO. This is clearly the case at Site 1230, where $\delta^{13}C_{DOL}$ is lower than −30‰. This is consistent with high production of CH_4 and the presence of gas hydrates at greater depth. Nevertheless, $\delta^{13}C_{DIC}$ is not as negative as the $\delta^{13}C_{DOL}$, which indicates that AMO may be episodic (see discussion below). Moreover, $\delta^{13}C_{DIC}$ and $\delta^{13}C_{DOL}$ at the shelf sites do not show any evidence for significant AMO. Also, CH_4 production is low at the shelf sites, with μM concentrations of CH_4, which is insufficient to account for most of the sulphate reduction through AMO. DNA studies by Parkes *et al.* (2005), Schippers & Neretin (2006) and Inagaki *et al.* (2006) show generally low amounts of Archaeal 16S rRNA genes and other groups, such as green non-sulphur bacteria, seem to be dominant at the SMI. However, based on the strongly varying $\delta^{13}C_{DOL}$ values, which reach in different depths much higher values than modern $\delta^{13}C_{DIC}$, methanogenesis was much higher in the past, and the high bacterial cell numbers observed at the SMI may be mainly dormant remains of a much more active SMI in the past. The dolomite could have incorporated a broad range of $\delta^{13}C$ values under non-steady-state conditions.

The dynamic deep biosphere

Different dolomite samples recovered in the sediments of the Peru margin during ODP Legs 112 and 201 show evidence of formation in the past at a shallower depth than their present position and, thus, document an evolution through most of the Pleistocene, which was influenced by a highly dynamic deep biosphere. The variations in $\delta^{13}C_{DOL}$ throughout the sedimentary sequences and the disequilibrium between the modern $\delta^{13}C_{DIC}$ and $\delta^{13}C_{DOL}$ imply shifts in the depth of the diagenetic zones, as well as dramatic variations of the rates of microbial activity through time. The positive $\delta^{13}C_{DIC}$ values in the methanogenic zone are mixed at the SMI with the negative values from the sulphate reduction zone and, after a shift in the redox zonation, a certain amount of time is required for the $\delta^{13}C_{DIC}$ value to come to a new equilibrium. By this mechanism, a range of different $\delta^{13}C_{DOL}$ values is possible at the SMI. Indeed, disequilibrium of the $\delta^{13}C_{DIC}$ values with modern redox zonation is observed at Site 1227 (Fig. 7A), which shows that even positive $\delta^{13}C_{DIC}$ values at the SMI are possible. At the shelf sites, the $\delta^{13}C_{DIC}$ values at the SMI do not indicate a high contribution of AMO and, thus, extremely negative $\delta^{13}C_{DOL}$ values are not expected. In contrast, strong AMO at the SMI in the trench Site 1230/685 is consistent with the observed extremely negative $\delta^{13}C_{DOL}$.

Based on the numeric model (Fig. 10), it is proposed that these changes are dominantly controlled by the activity of microbial sulphate reduction at specific intervals. S-shaped sulphate concentration profiles, measured at different sites, indicate active consumption at certain stratigraphic horizons at shallow depth. Numerical modelling shows that deposition of a 2·5 m thick organic carbon-rich layer, in which the sulphate reduction rate may reach 50 mmol m^{-3} a^{-1}, leads to a rapid removal of sulphate and a new SMI may be formed. The porewater sulphate model applied to Site 1229 demonstrates that, triggered by sulphate reducing activity in horizons with different organic matter content, the SMI may potentially migrate upwards from 30 to 5 mbsf and allow for dolomite precipitation at very shallow depths. For example, a shallow occurrence of dolomite was observed at Blake Ridge (Rodriguez *et al.*, 2000). Consumption of SO_4^{2-} may be horizontally restricted if the permeability is reduced, such as in clay-rich sediments. In such cases, more lense-shaped, nodular concretions would be expected, as observed in the Miocene Drakes Bay Formation, California (Burns *et al.*, 1988), whereas in porous diatom ooze, horizontal layers may form.

Dynamic activity of the deep biosphere may be triggered by different mechanisms. At the shelf sites, glacial–interglacial sea-level changes superimposed on tectonic uplift and subsidence may have a major effect on the diagenetic system by switching on and off the upwelling cell in the basin, which is reflected in strongly varying TOC concentrations in different intervals (Wefer *et al.*, 1990). The frequency of dolomite layers throughout the sedimentary

column of Site 1229 (Fig. 3) seems to correlate roughly with TOC concentration, as well as colour reflectance values (D'Hondt *et al.,* 2003) and the reconstructed bathymetry curve (determined by benthic foraminiferal assemblages, Resig, 1990). Thus, the SMI may have moved downwards during glacial lowstand, when microbial activity was low, and upwards during interglacial highstands, when microbial activity was high. This mechanism may explain the indirect coupling of dolomite formation with orbital cycles, as suggested by Compton (1988) based on the spacing of dolomite layers in the Monterey Formation. The formation of the layers was episodic and a massive layer can only form, when the site of precipitation is focused for a sufficient length of time.

Another mechanism was probably active at the trench site, where an extremely negative $\delta^{13}C_{DOL}$ value less than −30‰ was measured in a dolomite layer at 5 mbsf. This indicates intense AMO in the past, but the modern porewater $\delta^{13}C_{DIC}$ value only approaches −13‰. This increase in sulphate reduction and methane oxidation may have been triggered by decomposition of gas hydrates, possibly due to decompression during glacial sea-level lowstand. In an extreme case, the SMI might reach the sediment surface, causing seepage of methane into the seawater. Seep carbonates are common at both active and passive continental margins and show high variability of methane seepage through time (e.g. Thornburg & Suess, 1990). Variation in AMO was also proposed from the New Jersey continental shelf (Malone *et al.*, 2002), based on the disequilibrium between $\delta^{13}C_{Carbonate}$ and $\delta^{13}C_{DIC}$.

CONCLUSIONS

The study of the Peru Margin dolomites in a stratigraphic, geochemical and microbiological context provides strong evidence for formation in a highly dynamic environment, at shallow burial depths. The dolomite layers at the shelf and upper slope sites are formed in the uppermost 30 mbsf and, thus, document the evolution of the deep biosphere through time. A model for the control of deep-sea dolomite formation, where microbial activity causes dolomite precipitation at particular focused sites is proposed. 'Microbial hot-spots' with the highest bacterial cell counts, high metabolic activity and maxima in alkalinity were observed at the SMI, which also corresponds to the depth where Mg and Ca concentrations are at a minimum. Large variations in $\delta^{13}C_{DOL}$ would be consistent with dolomite formation at the SMI in a highly dynamic system. Increasing and decreasing microbial activity, including sulphate reduction and methanogenesis, would result in an upward or downward migration of the SMI. The upward migration may be triggered through TOC-rich layers produced by coastal upwelling during an interglacial highstand. To form a dolomite layer of significant thickness, however, requires that the SMI remains centred on the formation level for a relatively long period.

Further research in the context of future ocean drilling programs focused on sites of high microbial activity at biogeochemical interfaces may improve the understanding of the formation of early diagenetic minerals. Often, such minerals may contain the key to interpreting the palaeoconditions in ancient deep biospheres.

ACKNOWLEDGEMENTS

MaryLynn Musgrove is thankfully acknowledged for measuring the $\delta^{13}C$ values in the dissolved inorganic carbon. We especially thank Guy Simpson for helping with the numerical modelling of the sulphate concentrations. Discussions with Rolf Warthmann, Daniel Bernoulli, Robert Garrison, Will Berelson and Doug Hammond contributed significantly to the interpretations described in this study. We thank two anonymous reviewers for carefully reviewing this paper. Also, useful comments of George Claypool on an earlier version helped to improve the manuscript. This research used samples and data provided by the Ocean Drilling Program (ODP) and we thank the Leg 201 Shipboard Scientific Party for taking special care of sampling dolomite layers. Participating countries under the management of Joint Oceanographic Institutions (JOI), Inc. sponsored ODP. This study was financed by Swiss National Fund (SNF) Project No. 20-59282 and 20-67620 and ETH-Zürich. The SNF also sponsors the Swiss participation in ODP.

REFERENCES

Baker, P.A. and **Burns, S.J.** (1985) Occurrence and formation of dolomite in organic-rich continental margin sediments. *AAPG Bull.*, **69,** 1917–1930.

Baker, P.A. and **Kastner, M.** (1981) Constraints on the formation of sedimentary dolomite. *Science*, **213,** 214–216.

Bernoulli, D. and **Gunzenhauser, B.** (2001) A dolomitized diatomite in an Oligocene-Miocene deep-sea fan succession, Gonfolite Lombarda Group, northern Italy. *Sed. Geol.*, **139,** 71–91.

Bernoulli, D., Gasperini, L., Bonatti, E. and **Stille, P.** (2004) Dolomitization in pelagic limestone and diatomite, Romanche fracture zone, Equatorial Atlantic. *J. Sed. Res.*, **74,** 180–188.

Biddle, J.F., Lipp, J.S., Lever, M.A., Lloyd, K.G., Sørensen, K.B., Anderson, R., Fredericks, H.F., Elvert, M., Kelly, T.J., Schrag, D.P., Sogin, M.L., Brenchley, J.E., Teske, A., House, C.H. and **Hinrichs, K.-U.** (2006) Heterotrophic archaea dominate sedimentary subsurface ecosystems off Peru. *PNAS*, **103,** 3846–3851.

Boudreau, B.P. (1997) A mathematical model for sediment suspended particle exchange. *J. Mar. Syst.*, **11,** 279–303.

Burns, S.J. and **Baker, P.A.** (1987) A geochemical study of dolomite in the Monterey Formation, California. *J. Sed. Petrol.*, **57,** 128–139.

Burns, S.J., Baker, P.A. and **Showers, W.J.** (1988) The factors controlling the formation and chemistry of dolomite in organic-rich sediments: Miocene Drakes Bay Formation, California. In: *Sedimentology and Geochemistry of Dolostones* (Eds V. Shukla and P.A. Baker), *SEPM Spec. Publ. Tulsa*, **43,** 3–10.

Claypool, C.E. and **Kaplan, I.R.** (1974) The origin and distribution of methane in marine sediments. In: *Natural Gases in Marine Sediments* (Ed. I.R. Kaplan) , pp. 99–140. Plenum Press, New York.

Compton, J.S. (1988) Sediment composition and precipitation of dolomite and pyrite in the Neogene Monterey and Sisquoc Formations, Santa Maria Basin area, California. In: *Sedimentology and Geochemistry of Dolostones* (Eds V. Shukla and P.A. Baker), *SEPM Spec. Publ. Tulsa*, **43,** 53–64.

D'Hondt, S., Jørgensen, B.B., Miller, J. and **ODP Leg 201 Shipboard Scientific Party** (2003) Controls on microbial communities in deeply buried sediments, Eastern Equatorial Pacific and Peru Margin, Sites 1225–1231. In: *Proc. ODP Init. Rep.* (Eds L.L. Peters and P.H. Edwards), **201**: Ocean Drilling Program, College Station, TX.

D'Hondt, S., Jørgensen, B.B., Miller, J., Batzke, A., Blake, R., Cragg, B.A., Cypionka, H., Dickens, G.R., Ferdelman, T., Hinrichs, K.-U., Holm, N.G., Mitterer, R., Spivack, A., Wang, G., Bekins, B., Engelen, B., Ford, K., Gettemy, G., Rutherford, S.D., Sass, H., Skilbeck, C.G., Aiello, I.W., Guèrin, G., House, C.H., Inagaki, F., Meister, P., Naehr, T., Niitsuma, S., Parkes, J., Schippers, A., Smith, D.C., Teske, A., Wiegel, J., Padilla, C.N. and **Solis Acosta, J.L.** (2004) Distributions of microbial activities in deep subseafloor sediments. *Science*, **306,** 2216–2221.

Dickson, J.A.D. (1966) Carbonate identification and genesis as revealed by staining. *J. Sed. Petrol.*, **36,** 491–505.

Emeis, K.-C. and **Morse, J.W.** (1990) Organic carbon, reduced sulphur, and iron relationships in sediments of the Peru Margin, Sites 680 and 688. In: *Proc. ODP, Sci. Results* (E. Suess, R. von Huene *et al.*), **112,** pp. 413–440. Ocean Drilling Program, College Station, TX.

Friedman, G.M. (1965) Terminology of crystallisation textures and fabrics in sedimentary rocks. *J. Sed. Petrol.*, **35,** 643–655.

Garrison, R.E. and **Graham, S.A.** (1984) Early diagenetic dolomites and the origin of dolomite-bearing breccias, lower Monterey Formation, Arroyo Seco, Monterey County, California. In: *Dolomites of the Monterey Formation and Other Organic-rich Units* (Eds R.E. Garrison, M. Kastner and D.H. Zenger), *Pacific Sect. SEPM*, **41,** 87–101.

Hart, D. and **Miller, D.J.** (2006) Analysis and correlation of volcanic ash in marine sediments from the Peru Margin, Ocean Drilling Program Leg 201: explosive volcanic cycles of the North-Central Andes. *Proc. ODP Sci. Results*, **201,** Ocean Drilling Program, College Station, TX, published online: http://www-odp.tamu.edu/publications/201_SR/122/122.htm.

Horwitz, E.P., Dietz, M.L. and **Fisher, D.E.** (1991) Separation and preconcentration of strontium from biological, environmental, and nuclear waste samples by extraction chromatography using a crown-ether. *Anal. Chem.*, **63,** 522–525.

Inagaki, F., Nunoura, T., Nakagawa, S., Teske, A., Lever, M., Lauer, A., Suzuki, M., Takai, K., Delwiche, M., Colwell, F.S., Nealson, K.H., Horikoshi, K., D'Hondt, S. and **Jørgensen, B.B.** (2006) Biogeographical distribution and diversity of microbes in methane hydrate-bearing deep marine sediments on the Pacific Ocean Margin. *PNAS*, **103,** 2815–2820.

Kastner, M., Elderfield, H., Martin, J.B., Suess, E., Kvenvolden, K.A. and **Garrison, R.E.** (1990) Diagenesis and interstitial-water chemistry at the Peruvian Continental Margin – major constituents and strontium isotopes. In: *Proc. ODP, Sci. Results* (E. Suess, R. von Huene *et al.*), **112,** pp. 413–440. Ocean Drilling Program, College Station, TX.

Kelts, K. and **McKenzie, J.A.** (1982) Diagenetic dolomite formation in Quaternary anoxic diatomaceous muds of Deep Sea Drilling Project Leg 64, Gulf of California. In: *Initial Reports of the Deep Sea Drilling Project* (J.R. Curray, D.G. Moore et al.), **46,** pp. 553–569. Government Printing Office, Washington, DC.

Kelts, K. and **McKenzie, J.A.** (1984) A comparison of anoxic dolomite from deep-sea sediments: Quaternary Gulf of California and Messinian Tripoli Formation of Sicily. In: *Dolomites of the Monterey Formation and Other Organic-rich Units* (Eds R.E. Garrison, M. Kastner and D.H. Zenger), *Pacific Sect. SEPM*, **41,** 19–28.

Kulm, L.D., Schrader, H., Resig, J.M., Thornburg, T.M., Masias, A. and **Leonard, J.** (1981) Late Cenozoic carbonates on the Peru continental margin: lithostratigraphy, biostratigraphy, and tectonic history. In: *Nazca Plate: Crustal Formation and Andean Convergence* (L.D. Kulm, J. Dymond, E.J. Dasch, D. Hussong *et al.*), *Geol. Soc. Am. Mem.*, **154,** 469–504.

Kulm, L.D., Suess, E. and **Thornburg, T.** (1984) Dolomites in organic-rich muds of the Peru forearc basins: analogue to the Monterey Formation. In: *Dolomites of the Monterey Formation and Other Organic-rich Units* (Eds R.E. Garrison, M. Kastner and D.H. Zenger), *Pacific Sect. SEPM*, **41,** 29–47.

van Lith, Y., Warthmann, R., Vasconcelos, C. and **McKenzie, J.A.** (2003) Sulphate-reducing bacteria induce low-temperature Ca-dolomite and high Mg-calcite formation. *Geobiology*, **1,** 71–79.

Lumsden, D.N. (1979) Discrepancy between thin-section and X-ray estimates of dolomite in limestone. *J. Sed. Petrol.*, **49,** 429–435.

Malone, M.J., Claypool, G., Martin, J.B. and **Dickens, G.R.** (2002) Variable methane fluxes in shallow marine systems over geologic time: the composition and origin of pore waters and authigenic carbonates on the New Jersey shelf. *Mar. Geol.*, **189,** 175–196.

Mauclaire, L., Zepp, K., Meister, P. and **McKenzie, J.A.** (2004) Direct in situ detection of cells in deep-sea sediment cores from the Peru Margin (ODP Leg 201, Site 1229). *Geobiology*, **2/4,** p. 217, October 2004.

Meister, P., Prokopenko, M., Skilbeck, G., Watson, M. and **McKenzie, J.A.** (2005) Data report: compilation of total organic and inorganic carbon data from Peru Margin and Eastern Equatorial Pacific drill sites (ODP Legs 112, 138, and 201). *Proc. ODP Sci. Results*, **201,** Ocean Drilling Program, College Station, TX, published online: http://www-odp.tamu.edu/publications/201_SR/105/105.htm.

Meister, P., McKenzie, J.A., Warthmann, R. and **Vasconcelos, C.** (2006) Mineralogy and petrography of diagenetic dolomite from the ODP Leg 201 Peru Margin drill sites. *Proc. ODP Sci. Results*, **201,** Ocean Drilling Program, College Station, TX, published online: http://www-odp.tamu.edu/publications/201_SR/102/102.htm.

Murata, K.J., Friedman, I. and **Madsen, B.H.** (1969) Isotopic composition of diagenetic carbonates in marine Miocene formations of California and Oregon. *USGS Prof. Pap.*, **614-B,** 24.

Parkes, R.J., Webster, G., Cragg, B.A., Weightman, A.J., Newberry, C.J., Ferdelman, T.G., Kallmeyer, J., Jørgensen, B.B., Aiello, I.W. and **Fry, J.C.** (2005) Deep sub-seafloor prokaryotes stimulated at interfaces over geological time. *Lett. Nat.*, **436,** 390–394.

Pisciotto, K.A. and **Mahoney, J.J.** (1981) Isotopic survey of diagenetic carbonates. In: *Init. Rep. DSDP* (R.S. Yeats, B.U. Haq *et al.*), **63,** pp. 595–609. US Government Printing Office, Washington, DC.

Resig, J.M. (1990) Benthic foraminiferal stratigraphy and paleoenvironments off Peru. In: *Proc. ODP, Sci. Results* (E. Suess, R. von Huene *et al.*), **112,** pp. 263–296. Ocean Drilling Program, College Station, TX.

Rodriguez, N.M., Paull, C.K. and **Borowski, W.S.** (2000) Zonation of authigenic carbonates within gas hydrate-bearing sedimentary sections on the Blake Ridge: offshore southeastern North America. In: *Proc. ODP, Sci. Results* (Eds C.K. Paull, R. Matsumoto, P.J. Wallace and W.P. Dillon), **164,** pp. 301–312. Ocean Drilling Program, College Station, TX.

Rosenbaum, J. and **Sheppard, S.M.F.** (1986) An isotopic study of siderites, dolomites and ankerites at high temperatures. *Geochim. Cosmochim. Acta*, **50,** 1147–1150.

Schippers, A. and **Neretin, L.N.** (2006) Quantification of microbial communities in near-surface and deeply buried marine sediments on the Peru continental margin using real-time PCR. *Environ. Microbiol.*, **2006,** 1–10.

Schippers, A., Neretin, L.N., Kallmayer, J., Ferdelman, T., Cragg, B.A., Parkes, R.J. and **Jørgensen, B.B.** (2005) Prokaryotic cells of the deep sub-seafloor biosphere identified as living bacteria. *Lett. Nat.*, **433,** 861–864.

Schulz, H.D. and **Zabel, M.** (2000) *Marine Geochemistry*. Springer-Verlag, Berlin.

Suess, E., von Huene, R. and **ODP Leg 112 Shipboard Scientific Party** (1988) Peru continental margin. In: *Proc. ODP Init. Rep.*, **112,** pp. 1015. Ocean Drilling Program, College Station, TX.

Thornburg, T.M. and **Suess, E.** (1990) Carbonate cementation of granular and fracture porosity: implications for the cenozoic hydrologic development of the Peru Continental Margin. In: *Proc. ODP, Sci. Results* (E. Suess, R. von Huene *et al.*), **112,** pp. 95–109. Ocean Drilling Program, College Station, TX.

Vasconcelos, C., McKenzie, J.A., Bernasconi, S., Grujic, D. and **Tien, A.J.** (1995) Microbial mediation as a possible mechanism for natural dolomite formation at low temperatures. *Nature*, **377,** 220–222.

Vasconcelos, C., McKenzie, J.A., Warthmann, R., Bernasconi, S. (2005) Calibration of the $\delta^{18}O$ paleo-thermometer with dolomite formed in microbial cultures and natural environments. *Geology*, **33,** 317–320.

Veizer, J., Ala, D., Azmy, K., Bruckschen, P., Buhl, D., Bruhn, F., Carden, G.A.F., Diener, A., Ebneth, S., Godderis, Y., Jasper, T., Korte, G., Pawellek, F., Podlaha, O.G. and **Strauss, H.** (1999) $^{87}Sr/^{86}Sr$, $\delta^{13}C$ and $\delta^{18}O$ evolution of Phanerozoic seawater. *Chem. Geol.*, **161,** 59–88.

Visscher, P.T., Reid, R.P. and **Bebout, B.M.** (2000) Microscale observations of sulfate reduction: correlation of microbial activity with lithified micritic laminae in modern marine stromatolites. *Geology*, **28,** 919–922.

Warthmann, R., van Lith, Y., Vasconcelos, C., McKenzie, J.A. and **Karpoff, A.-M.** (2000) Bacterially induced dolomite precipitation in anoxic culture experiments. *Geology*, **28,** 1091–1094.

Wefer, G., Heinze, P. and **Suess, E.** (1990) Stratigraphy and sedimentation rates from oxygen isotope composition, organic carbon content, and grain-size distribution at the Peru upwelling region: holes 680B and 686B. In: *Proc. ODP, Sci. Results* (E. Suess, R. von Huene *et al.*), **112,** pp. 355–367. Ocean Drilling Program, College Station, TX.

Manuscript received 24 July 2006; revision accepted 5 February 2007